Confined-Plume Chemical Deposition of Transition Metal Borides and Chalcogenides Initiated by Pulsed, Infrared, Tabletop Lasers

By

Jeremiah Cooper Beam

Dissertation
Submitted to the Faculty of the
Graduate School of Vanderbilt University
in partial fulfillment of the requirements
for the degree of

DOCTOR OF PHILOSOPHY
in

Chemistry
May, 2016
Nashville, Tennessee

Approved: Date:

Charles M. Lukehart, Ph.D.; Chair

David E. Cliffel, Ph.D.

Timothy P. Hanusa, Ph.D.

Borislav L. Ivanov, Ph.D.

David W. Wright, Ph.D.

To Mom and Dad,

For never giving up on me

ACKNOWLEDGEMENTS

I would first and foremost like to thank Dr. Charles M. Lukehart for all his patience, knowledge and support over the last several years. His guidance throughout this entire process has been much appreciated. I am also grateful of the freedom I was given to explore research areas outside of my main project. Additionally, I would like to thank Profs. David Cliffel, Timothy Hanusa and David Wright not only for their support, but also the use of laboratory space and equipment as our lab moved all over Stevenson Center.

I would also like to acknowledge Prof. Borislav Ivanov for all of his assistance. We've had many philosophical discussions and arguments while performing experiments, and I have learned a lot from them. I truly wouldn't be at this position without his knowledge and support.

This work is the result of many successful collaborations across many different fields. Dr. John Kozub has been essential in the completion of this research and has been very patient with our equipment needs. Prof. Kane Jennings, Dr. Gabriel LeBlanc, and Evan Gizzie were instrumental in the successful completion of the ZnO/PSI project. Evan and Dr. David Crisostomo are also acknowledged for their continuing assistance with electrochemical testing. Profs. Alex Papandrew, Gabriel Goenana and Tom Zawodzinski at UT-Knoxville also helped with some of the electrochemical testing on the tantalum oxide project. I would also like to thank Jennifer Pickering for allowing me to work on a geology project, which has helped me broaden my scientific knowledge and also helped me better understand an instrument I work with on a daily basis.. Lastly, Prof. Lizhi Ouyang and Dr. Ranganathan Parthasarathy at Tennessee State University have been essential in the adhesion studies of our ReB_2 films.

To my friends: Anna, Bobby, Dave, Evan, Jenny, Keersten, Nick and Wes, getting to know you all these past several years has been a great experience, I wouldn't have lasted a year without you all. From the board game sessions, business lunches and nights at the bar, I could not ask for a better set of people to go through this experience with.

I would also like to thank Vanderbilt Unversity, NSF EPSCoR and Savannah River National Laboratory for financial support. Additionally, I would like to thank Profs. Tony Hmelo, Dmitry Koktysh, James McBride and Dr. Ben Schmidt for their amazing help with ViNSE instrumentation and training.

Last, but certainly not least, I would like to thank my family for all their love and support over the last six years. They have always supported and believed in me, even when I started to doubt myself, and for that I am forever grateful.

TABLE OF CONTENTS

Page

LIST OF TABLES

Table Page

Chapter II

LIST OF FIGURES

Figure Page

Chapter I

Chapter II

Chapter III

Foreword

The water, food and energy nexus has been a driving force for research and development in many areas of science and engineering. As the world's population increases and humans demand higher quality of life, we put strain on all three areas of the nexus. Access to clean water is necessary for the production of food, for sustenance, sanitation, and in some cases the production of energy. This puts strain on the need for more energy to purify the water needed for these tasks and puts a strain on food security if water is being used in other industries.

An increase in the demand for food places strain on water security as agriculture is currently responsible for around 70% of the total water usage. Additionally, more energy is needed to produce fertilizer, run farming equipment, and transporting food to the masses.

As we increase the demand for energy, it puts a strain on water security as we use water in the processing of some forms of energy. Food is also strained as we can use our food supply to generate energy in the form of biofuels.

Attacking this nexus from one research area can have consequences that result in the reduction of strain at another point, giving the research far reaching benefits in an area it does not pertain to.

The research described within this dissertation focuses on energy-related materials. In chapter I, a new synthesis technique is described which not only is capable of producing energy generation devices, but also offers an alternative to current energy inefficient processes. Using our current sources of energy efficiently also reduces strain on the nexus.

Chapter II approaches the energy problem from a more traditional source. Alternative energy sources have long been sought to replace our finite supply of fossil fuels. Solar power and renewable biofuels have long been researched as a possible alternative to fossil fuel based energy sources. We have successfully synthesized catalysts that function to break down some of these biofuels, like methanol and formic acid, and produce energy using a fuel cell.

Lastly, chapter III focuses on a topic outside of our traditional research and looks at the geochemical makeup of a river delta. The knowledge gained from this study allows us a glimpse of the Earth thousands of years in the past and see how time and environmental processes has changed the makeup and face of our planet, perhaps giving us a chance to predict what will happen in the future.

Science is the collection of knowledge gathered over the period of hundreds of thousands of lifetimes, everything that has been discovered up to this day will be used now and in the future to guide researchers in their quest for answers.

Chapter I: Confined-Plume Chemical Deposition of Transition Metal Borides and Chalcogenides Initiated by Pulsed, Infrared, Tabletop Lasers

Introduction

Confined-Plume Chemical Deposition

In chemical vapor deposition (CVD), a volatile precursor is vaporized and passed through a heated chamber where decomposition occurs onto a target substrate. This process easily produces high-purity materials.[1–4] One requirement for CVD precursors is volatility at room temperature and atmospheric pressure. While there are a large number of precursors that meet this requirement, many materials are not able to be synthesized by this method due to the lack of a suitably volatile precursor.

In physical vapor deposition, a target consisting of the desired material is acted upon by a physical process, such as sputtering or heating, which results in the formation of a vapor.[5,6] The vapor then is deposited on the substrate of choice. While efficient, the deposition of this material is wasteful, as it also coats the interior of the chamber the vapor is contained in and does not guarantee the formation of a crystalline product.

Most of these techniques require the use of specialized vacuum equipment, inert atmospheres, and volatile precursors to achieve uniform deposition. Additionally, obtaining crystalline materials deposition requires the heating of the substrate, precluding deposition on temperature sensitive substrates such as polymers and biological tissue. A deposition method that can be performed under ambient conditions and obtain crystalline materials is therefore sought.

Confined-plume chemical deposition solves a majority of these problems.[7] In CPCD, a precursor is physically confined between two substrates. The top substrate must be

transparent to the incident irradiation wavelength, while the bottom substrate is where the bulk of the deposition occurs. This assembly is then exposed to resonant irradiation from a pulsed laser. The laser is tuned to a vibrational mode found in the molecular precursor. The absorption initiates the formation of a reaction plume, from which crystalline materials nucleate and grow from the substrate surface **(Figure 1)**. Attempts to

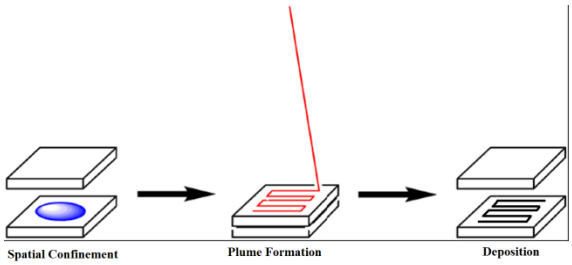

Figure 1. Cartoon depiction of CPCD processing

induce decomposition by off-resonant wavelengths results in no decomposition of precursor molecules. The pulsed nature of the incident beam temporally confines the plume and results in the rapid dissipation of thermal energy throughout the substrate material, resulting in no noticeable collateral thermal damage. This process was initially demonstrated using a free-electron laser, a tunable infrared source. Although the initial experiments were successful in depositing crystalline material on polymer substrates, the lack of widespread access to FEL facilities led researchers to adapt this technique to be demonstrated on tabletop lasers, which are found at most research institutions across the world.

Among the tabletop lasers available at Vanderbilt are an 800-nm Ti:Sapphire laser, which operates at a power of 1 W, with a pulse duration of 130 fs and repetition rate of 1 kHz. Another laser, a 527-nm Nd: YLF source, operates with a maximum power of 6 W, with

a pulse duration of 150 ns, and a repetition rate of 1 KHz. Additionally, an infrared 2.94-μm Er:YAG dental laser, with a maximum energy of 300 J, with a pulse duration of 150 μs and a repetition rate of up to 20 Hz is available. The three available wavelengths, vastly different energies and pulse durations allow the applicability of this technique to be confirmed under a wide set of parameters.

Superhard Materials

Superhard materials are defined as a material with a bulk modulus of over 40 GPa. These materials have many applications in the area of cutting and wear resistant tools. The resistance of these materials to compress or deform is thought to be related to the degree of covalent character of the bonds in the material. Examples of superhard materials are diamond, B_4C, c-BN, OsB_2, WB_4 and ReB_2.[8,9,10] Diamond, the strongest material known, is commonly used as a coating for cutting blades, but is not used to cut ferrous materials. Cutting an iron-containing material with a diamond blade results in the formation of brittle iron carbide. Boride materials are more desirable for the cutting of ferrous materials as iron boride phases are not stable.

ReB_2 has been synthesized by a number of routes, including arc-melting of rhenium and boron powders at high temperature, but this reaction takes place over a period of 5 days.[11,12] Therefore a rapid synthesis route for ReB_2 production is desired.

Semiconducting Materials

The semiconductor industry has grown rapidly since the discovery of the transistor in 1947. Current semiconductor research is spread across many areas including computers and photovoltaic power generation.[13,14] Semiconductors are desirable materials due to the

ability to dope the pure material and thereby change its electronic properties. Silicon, especially, is known for the ease of which it can be doped to either n-type (e.g. phosphorus, arsenic) or p-type (e.g. boron). In photovoltaic devices, controlling the band energy of a semiconductor material is essential to allow electrons to be accepted and donated throughout the device.

ZnO is an intrinsically n-doped semiconductor with a band gap of 3.3 eV. Additionally, it is a piezoelectric material, which allows it to be used in piezoelectric devices, in which mechanical strain can be harvested as electrical energy.[15–18] It can be synthesized by a number of methods, including hydrothermally, atomic layer deposition, or electrolysis.[19] However, most of these synthetic methods result in either low deposition rates or require high temperatures. [20]

Photosynthesis Based Photochemical Electrical Generation

Over the course of billions of years of evolution, nature has created a robust and efficient means to convert solar energy to chemical energy. Photosynthetic proteins found in plants and algae are capable of photoexciting electrons from the P700 reaction center, a modified chlorophyll, to a set of redox centers consisting of iron-sulfur clusters at the F_B site. A water-soluble protein, known as ferredoxin, is able to accept this electron, while the hole generated in the P700 reaction enter is filled by another protein, plastocyanin.[21] By replacing the redox centers with other electrochemical mediators, we are able to hijack the photosynthetic pathway and use photoexcited electrons to generate electricity.

In addition to electrochemical mediators, semiconducting materials are also capable of accepting this photoexcited electron, while other semiconductor, such as p-doped silicon,

are able to fill the hole generated at the P700 reaction center. This combination of inorganic and biological components leads to a biohybrid photosynthetic device.

When constructing a device based around a p-doped silicon/PSI substrate, the electron accepting semiconductor must be transparent to visible light to allow the photoexcitation to occur. ZnO has been shown to aceept electrons from the F_B site and as a large band gap material, is also transparent to visible light. While ZnO is a suitable material for these types of devices, deposition of ZnO onto a biological material composes several challenges. Firstly, most deposition of ZnO is accomplished by hydrothermal processing in which termperatures exceed 80 °C. Exposure of the protein to these temperatures is likely to denature it with the loss of its photoactivity. Secondly, the semiconducting ZnO must have sufficient contact with the protein as to be able to accept its electron. CPCD offers a method that is capable of deposition under mild conditions, allowing the protein to remain photoactive and offers good contact between the substrate and semiconducting material. Using CPCD initiated by a 2.94-μm tabletop Er:YAG laser, we have constructed a robust ZnO/PSI interface and generated a solid-state biohybrid photoelectrochemical device.

Experimental Methods

General Considerations

X-ray diffraction patterns were collected on a Scintag X-1 Powder X-ray Diffractometer equipped with a copper target and a Peltier cooled solid-state detector. Scanning electron microscopy images were collected on a Hitachi S4200 scanning electron microscope at 10 kV accelerating voltage. Energy dispersive x-ray spectra were collected at 20 keV. Raman spectra were collected on a Thermo Scientific DXR Confocal Raman Microscope (532 nm, 2 mW).

Synthesis of $Re(CO)_5Br$[22]

Under a nitrogen atmosphere, $Re_2(CO)_{10}$ (1.5 g, 2.3 mmol) was dissolved in 50 mL dichloromethane. Then, bromine was added dropwise until the color persisted. This solution was stirred for 30 minutes, then the solvent and excess bromine were removed by rotary evaporation. A white solid, $Re(CO)_5Br$, was collected.

Synthesis of CsB_3H_8[23]

In a 3-neck flask equipped with a magnetic stirring bar and under a nitrogen atmosphere, $NaBH_4$ is dissolved in dry, distilled 250 mL diglyme (bis(2-methoxyethyl) ether) and heated to 100 °C. Meanwhile, iodine is dissolved in 125 mL diglyme in a separate flask under a nitrogen atmosphere. When the $NaBH_4$ solution has reached 100 °C, an addition funnel is placed into one of the necks of the flask, and the iodine solution is added to it. A gas bubbler charged with 2-picoline is placed in the last neck, and nitrogen flow is stopped (2-picoline will react with any diborane that escapes the reaction flask). The iodine solution is then slowly introduced to the $NaBH_4$ solution at a rate of about 1 mL per minute so that the entire addition is complete over 2 hours.

Once the addition of the iodine is complete, the solution is stirred an additional 1.5 hours. The flask contents are transferred to a 1-neck flask and the solvent is removed by rotary evaporation at 100 °C. The flask is then allowed to cool to room temperature. The solid is extracted with 50-mL portions of diethyl ether until the solvent is colorless. 1,4-dioxane is then added to the collected ether solution to precipitate $NaB_3H_8 \cdot 3\ C_4H_8O_2$. The solid dioxane is then added to a 1 L solution of CsBr in water, with a 10% excess of CsBr. A white powder precipitates from this solution and is filtered and dried to yield CsB_3H_8.

Synthesis of $Re(CO)_4B_3H_8$[22]

A quartz Schlenk flask is charged with a magnetic stirring bar and about 20 1 mm glass beads. The flask is purged with nitrogen through the use of a needle. Then, $Re(CO)_5Br$ (1.0 g, 2.5 mmol) and CsB_3H_8 (0.500 g, 2.8 mmol) are added along with 30 mL methylene chloride. The Schlenk flask is then fitted with a reflux condenser and a gas bubbler. The reaction solution is purged with nitrogen throughout the reaction. The flask is irradiated with a mercury vapor lamp with maximum emission around 254 nm, for 72 hours. The flask contents are then transferred to a 3-neck round bottom flask and the methylene chloride is removed under reduced pressure and the product, $Re(CO)_4B_3H_8$, a colorless liquid, is collected under high vacuum (< 1 mtorr) at -40 °C (dry ice/acetonitrile) in a pear shaped flask.

Synthesis of ReB_2 by Confined-Plume Chemical Deposition

1 drop of $Re(CO)_4B_3H_8$ is placed onto a substrate of choice and confined by a sapphire wafer using an IR-spectroscopy pellet holder or a custom aluminum frame. The multilayer specimen is then mounted to an X-Y stage and passed through a cylindrically focused laser beam. The laser source is either an 800-nm Ti:Sapphire source with a power of 1 W, pulse length of 130 fs and a repetition rate of 1 KHz, or a 527-nm frequency doubled Q-switched Nd:YLF source with a power of 3.5 W, pulse length of 100 ns and a repetition rate of 1 KHz. The specimen is scanned though the laser beam at a rate of 100 μm/sec until the precursor layer is completely converted, typically 7-10 times. The sapphire wafer is removed to reveal a black deposition on the bottom substrate along the path of the laser beam.

Mechanical Testing of ReB_2/PTFE composites

Nanoindentation data was collected on an Agilent G200 nanoindenter with a Berkovich pyramid tip and a load of 50 μN. Adhesion data was determined using a Deben Microtester. Dogbone samples of PTFE were stamped from a sheet of PTFE and coated with ReB_2 by CPCD as described above. The dogbones were then cut into smaller pieces roughly 0.125" x 0.5" and the uncoated side was sanded with 100-grit sandpaper and etched with a fluoropolymer etchant. This sanded and etched side was then glued to another sanded and etched piece of PTFE with RealTek BondIt-4811 and cured in ambient conditions for 36 hours. Another dogbone piece was sanded and etched and adhered to the ReB_2 coated face with RealTek BondIt-4811 and cured for 36 hours.

After curing, the dogbone assembly was loaded into a Deben Microtester and a 200 N load was applied and displacement occurred at a rate of 0.1 mm/min. Force/strain curves were generated and the adhesion strength of the coating to the polymer was determined. Additional samples were prepared with the PTFE surface being etched before the deposition of ReB_2 occurred.

Synthesis of $Mn(CO)_5Br$[24]

Under a nitrogen atmosphere, $Mn_2(CO)_{10}$ (1.5 g, 3.8 mmol) was dissolved in 50 mL carbon tetrachloride. Then, bromine was added dropwise until the bromine color persisted. This solution was stirred at 40 °C for 30 minutes, then the solvent and excess bromine were removed by rotary evaporation. A yellow solid, $Mn(CO)_5Br$, is collected.

Synthesis of $Mn(CO)_4B_3H_8$[25]

A quartz Schlenk flask is charged with a magnetic stirring bar and about 20 1-mm glass beads. The flask is purged with nitrogen through the use of a needle. Then, $Mn(CO)_5Br$ (1.0 g, 3.6 mmol) and CsB_3H_8 (0.717 g, 4.1 mmol) are added along with 30 mL methylene chloride. The Schlenk flask is then fitted with a reflux condenser and a gas bubbler. The reaction solution is purged with nitrogen throughout the reaction. The flask is irradiated with a mercury vapor lamp with maximum emission around 254 nm, for 72 hours. The flask contents are then transferred to a 3-neck round bottom flask and the methylene chloride is removed under reduced pressure and the product, $Mn(CO)_4B_3H_8$, a red-orange liquid, is collected under high vacuum (< 1 mtorr) at -40 °C (dry ice/acetonitrile) in a pear shaped flask.

Synthesis of $Zn_5(OH)_6(CO_3)_2$[26]

Under a nitrogen atmosphere, 25 mL dry tetrahydrofuran is added to a three-neck flask. N-propylamine (1.50 mL, 1.08 g, 18 mmol) is then added along with 3.6 mL of a 5.0 M n-butyl lithium solution in diethylether. The solution is stirred for 30 minutes, and then carbon dioxide is bubbled into the solution for 15 minutes. Then a solution of $ZnCl_2$ in water is added to the solution and a white solid, $Zn_5(OH)_6(CO_3)_2$, precipitates. The solution is filtered and washed with water, and the white solid is dried at 50 °C in an oven overnight.

Extraction of Photosystem I[27]

Thylakoid membranes were isolated from spinach leaves via maceration and subsequent centrifugation at 4000 g. The PSI complex was then removed from the thylakoid membrane by adding a high concentration of surfactant, followed by further

centrifugation. The protein was then purified using a chilled hydroxyapatite column. Following elution, excess surfactant and salt were removed via dialysis.

Synthesis of ZnO/Photosystem I/p-doped Silicon by Confined-Plume Chemical Deposition

10 mg $Zn_5(OH)_6(CO_3)_2$ is suspended in 1 mL benzene and 10 μL of this solution is dropcast onto a layer of photosystem I that had been deposited on p-doped silicon and confined with a glass microscope slide. The multilayer specimen is then placed in an IR spectroscopy pellet holder, or a custom aluminum frame. This frame is then mounted to an X-Y stage and scanned through a 2.94-μm Er:YAG laser with an energy of 100 mJ, pulse length of 100 μs and a repetition rate of 20 Hz that has been focused through a cylindrical ZnSe lens. The sample is passed through the laser twice at a rate of 300 μm/sec. The glass slide is removed to reveal a translucent white film on the substrate.

Photoelectrochemistry of ZnO/PSI/p-doped Silicon multilayers

Photoelectrochemical measurements were performed using a CH Instruments CHI 660A electrochemical workstation. The silicon substrate was set as the working electrode, with Ag/AgCl (3M KCl) as the reference electrode and platinum mesh as the counter electrode. Electrochemical mediator solutions consisted of 100 mM potassium chloride, and either 2 mM hexaaminеruthenium(III) chloride or 2 mM methyl viologen dichloride hydrate.

Solid-state Device Fabrication

Solid-state devices were fabricated using indium tin oxide-coated polyethylterephthlate (ITO-PET) (60 Ω $square^{-1}$) to make electrical contact with the ZnO layer. To generate as much contact as possible, a small piece of PET was pressed onto the

flexible ITO electrode by sandwiching the layers between two pieces of glass and binding the system together with clips. Photochronoamperometric experiments were performed at an applied potential of 0.0 V (vs. Ag/AgCl). Illumination was provided using a 250 W cold light source equipped with a 633-nm high-pass filter generating a light intensity of 0.19 W/cm^2.

Current-Voltage Measurements at Solar Simulation

i-V curves for solid-state devices were obtained using a solar simulator with an AM1.5G filter connected to a Keithley 2400 source meter controlled by a custom-designed Labview program. The samples were swept from -0.5 to 0.5 V at a step rate of 0.02 V. The lamp was calibrated to 1.00 full sun with a NREL certified silicon reference diode.

Synthesis of $Cd[S_2CN(CH_2CH_2CH_3)H]_2$[28]

Under a nitrogen atmosphere, 25 mL dry tetrahydrofuran is added to a three neck flask. N-propylamine (0.938 mL, 0.638 g, 11 mmol) is then added along with 2.3 mL of a 4.6 M n-butyl lithium solution in diethylether. The solution is stirred for 30 minutes, then carbon disulfide is added to the solution. Then a solution of $CdCl_2$ in water is added to the solution and a yellow solid, $Cd[S_2CN(CH_2CH_2CH_3)H]_2$, precipitates. The solution is filtered and washed with water, and the yellow solid is dried at 50 °C in an oven overnight.

Synthesis of CdS by Confined-Plume Chemical Deposition

5 mg $Cd[S_2CN(CH_2CH_2CH_3)H]_2$ is sprinkled onto the substrate of choice and confined with a glass microscope slide. The multilayer specimen is then placed in an IR spectroscopy pellet holder, or a custom aluminum frame. This frame is then mounted to an X-Y stage and scanned through an 800-nm Ti:Sapphire source with a power of 1 W, pulse

length of 130 fs and a repetition rate of 1 KHz or 2.94-μm Er:YAG laser with an energy of 100 mJ, pulse length of 150 μs and a repetition rate of 20 Hz that has been focused through a cylindrical ZnSe lens. The sample is passed through the laser twice at a rate of 300 μm/sec. The glass slide is removed to reveal a translucent yellow film on the substrate.

Results and Discussion

Confined-Plume Chemical Deposition of ReB_2 films using 800-nm and 527-nm pulsed, tabletop, laser irradiation

When multilayer assemblies containing $Re(CO)_4B_3H_8$ are exposed to femtosecond pulsed irradiation from a 527-nm or 800-nm tabletop laser, CPCD proceeds by the formation of a reaction plume originating at the precursor layer. After initial plume formation, the sample is scanned through the laser beam, causing the reaction plume to propagate throughout the rest of the sample. The reaction plume will persist until the precursor layer is exhausted. From this reaction plume, microcrystalline platelets of ReB_2 nucleate and grow from the surface of the substrate. The pulsed nature of the beam allows thermal energy to rapidly dissipate throughout the substrate material, resulting in no noticeable collateral thermal damage to the substrate. Removal of the sapphire wafer reveals a black deposit on the bottom substrate, with a small amount of deposition on the sapphire itself. XRD analysis of this film indicates the formation of ReB_2 as the major crystalline product, with a small amount of B_2O_3 also present **(Figure 2)**. The presence of B_2O_3 is expected as the precursor contains an excess of boron which rapidly oxidizes. Raman analysis is also consistent with the formation of ReB_2, with a peak around 768 cm^{-1} which corresponds to the B-B out of plane vibration **(Figure 3).** Additionally, two broad peaks are seen at 1373 and 1588 cm^{-1}, which are consistent with D- and G- bands of sp^2-

hybridized carbon, respectfully. This carbon originates from the decomposition of the carbonyl ligands in the precursor molecule as there is no other source of carbon in the ReB_2/glass system; carbon has previously been noted from the thermal decomposition of $W(CO)_6$.[12] SEM analysis of this sample shows a uniform field of thin platelets across the entire substrate **(Figure 4)**.

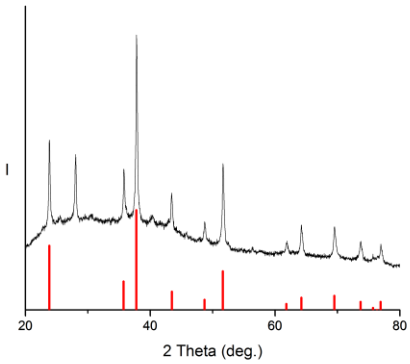

Figure 2. XRD pattern of ReB_2/glass, red drop lines are that of bulk ReB_2 (PDF#11-0581)

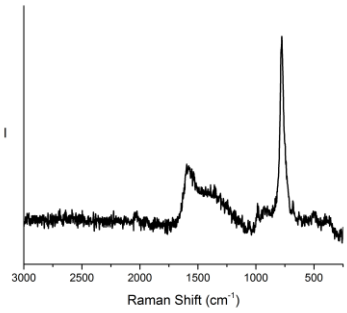

Figure 3. Raman spectra of ReB_2/glass. Peak at 768 cm^{-1} is assigned to the B-B out of plane vibration of ReB_2, while peaks at 1373 and 1588 cm^{-1} are assigned to D- and G-band of carbon, respectively.

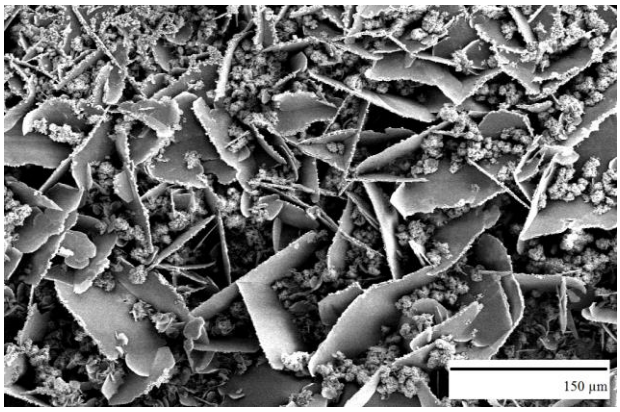

Figure 4. SEM image of ReB_2/glass, showing platelet formation

With confirmation that CPCD is possible on a tabletop laser, we sought more evidence that there is little or no collateral thermal damage to the substrate. By replacing the glass substrate with high density polyethylene (HDPE) and poly(tetrafluoro)ethylene (PTFE), we hoped to create a robust interface between the crystalline ceramic ReB_2 layer and the polymer surface, which cannot be created by any other deposition technique. XRD analysis of ReB_2/HDPE composites indicates much the same as ReB_2/glass samples. ReB_2 is the major crystalline product formed, as well as a small amount of B_2O_3 **(Figure 5)**. In addition, SEM and Raman analysis are consistent with the morphology and Raman shift of the glass samples, indicating no difference in the deposition when the substrate is changed **(Figures 6 and 7)**. The PTFE samples again follow this same trend **(Figures 8-10)**.

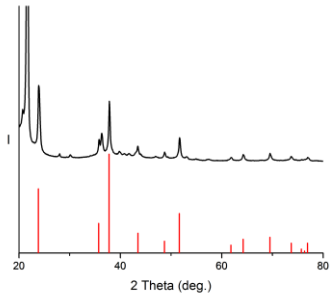

Figure 5. XRD pattern of ReB_2/HDPE. Red drop lines indicate pattern of bulk ReB_2 (PDF # 11-0581).

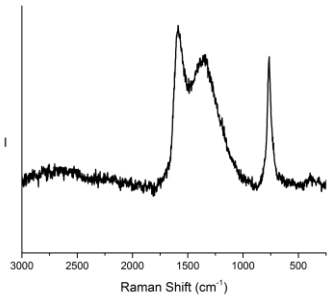

Figure 6. Raman spectrum of ReB_2/HDPE

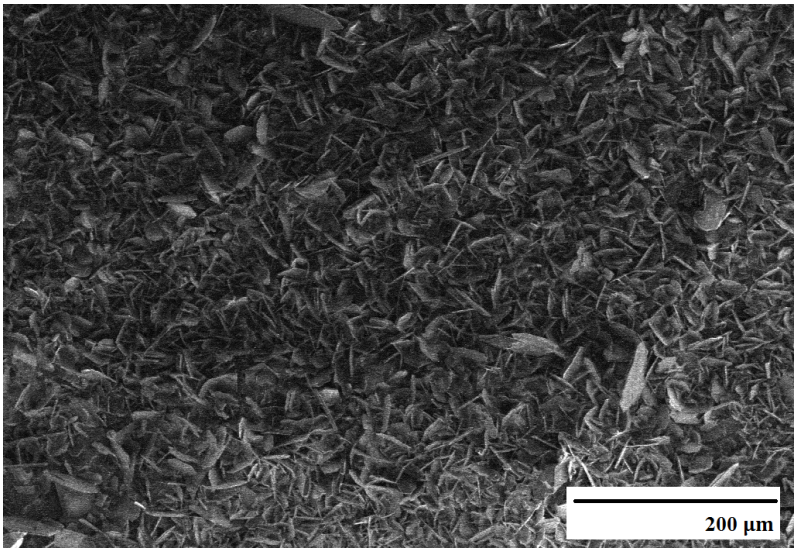

Figure 7. SEM image of ReB_2/HDPE

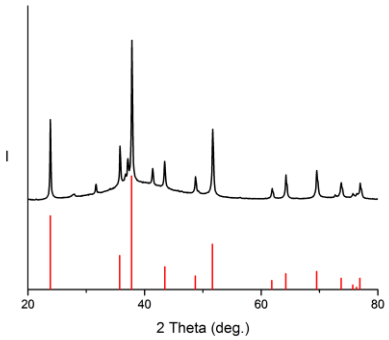

Figure 8. XRD pattern of ReB_2/PTFE. Red drop lines indicate pattern of bulk ReB_2 (PDF # 11-0581).

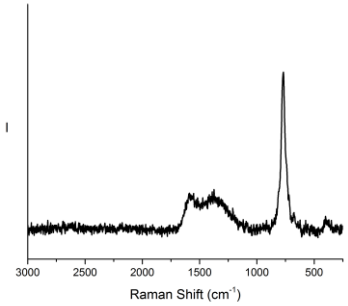

Figure 9. Raman spectrum of ReB_2/PTFE

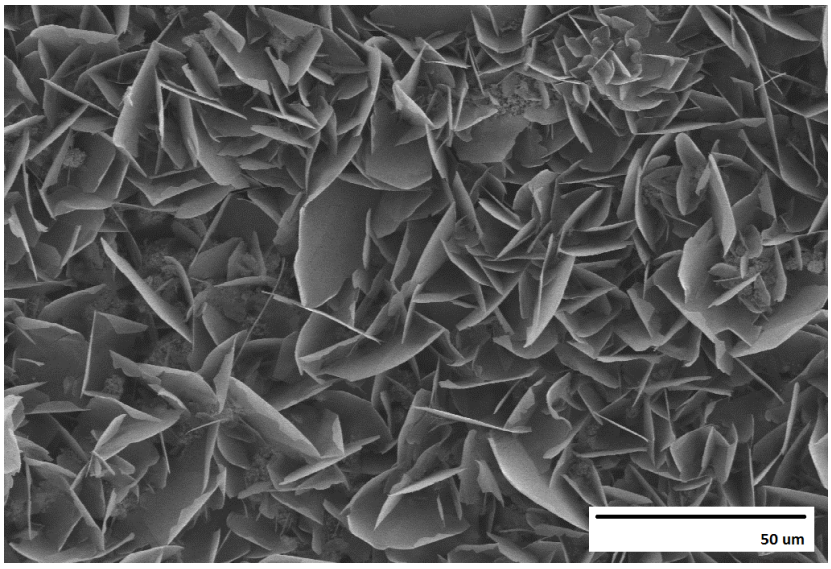

Figure 10. SEM image of ReB_2/PTFE

Using a 527-nm source, ReB_2 was also deposited on a bone cross section collected from a domestic cow femur. The use of another wavelength to initiate plume formation adds to the breadth of CPCD. Deposition occurs in much the same way as using the 800-nm source, but the concentration of platelets seen on the bone surface is much lower than seen on any other substrate **(Figure 11).** The lower light intensity from the 527-nm laser in comparison to the 800-nm laser could lower the amount of nucleation events that occur, leading to lower coverage of the film. Addtionally, this could be due to the porosity of the bone, where the liquid precursor is infiltrating these pores and nucleating and growing from the interior. XRD analysis indicates that ReB_2 is the only crystalline product **(Figure 12).** SEM analysis shows a sparse coating of platelets but is the bone is visibly black, indicating deposition does occur at every point on the surface.

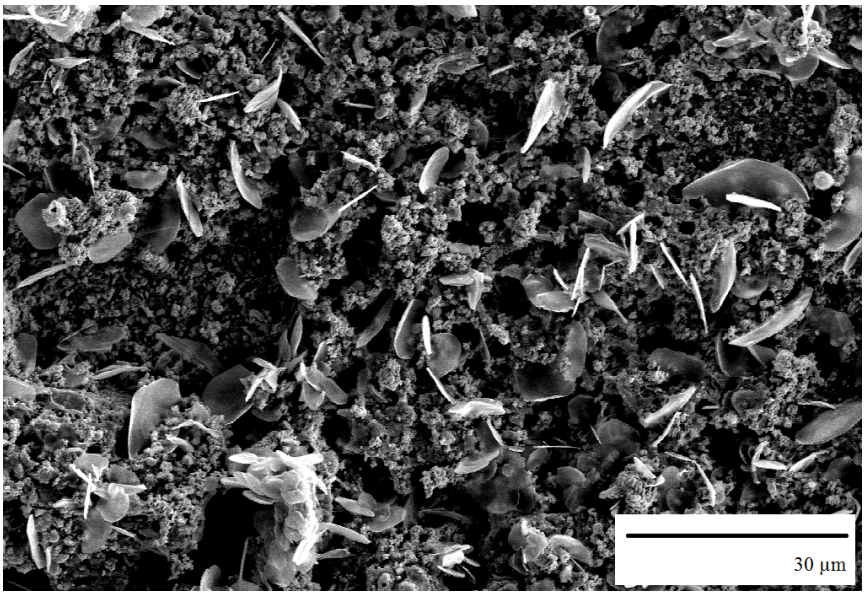

Figure 11. SEM image of ReB_2/bone initiated by a 527-nm laser

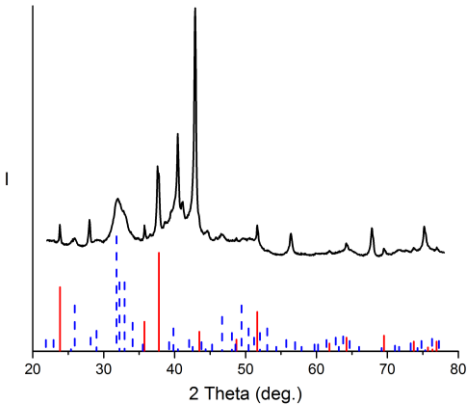

Figure 12. XRD pattern of ReB_2/bone. Red drop lines indicate bulk ReB_2 (PDF#11-0581), Blue dashed lines indicate bulk hydroxyapatite (PDF#09-0432)

Analysis of ReB_2/PTFE Adhesion Strength

Nanoindentation of ReB_2/PTFE samples revealed an interesting result **(Figure 13)**. The control PTFE sample and scanned PTFE had virtually identical bulk modulus, which indicates that scanning the polymer under the laser does not affect its mechanical properties. Additionally, when ReB_2 is coated on the PTFE surface, the bulk modulus increases by about 170%. However, this is much lower than the bulk modulus of ReB_2. The aspect ratio of the platelets, which are thin relative to their size, might interact with the pyramid during indentation and not increase the overall hardness of the composite.

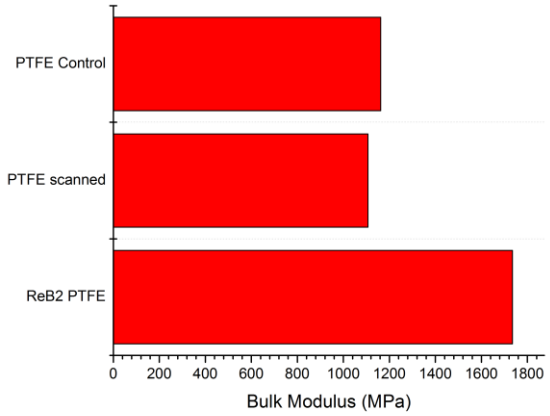

Figure 13. Nanoindendation data for ReB_2/PTFE. PTFE control has not been modified prior to testing, PTFE scanned was exposed to 10 passes of the 800-nm laser.

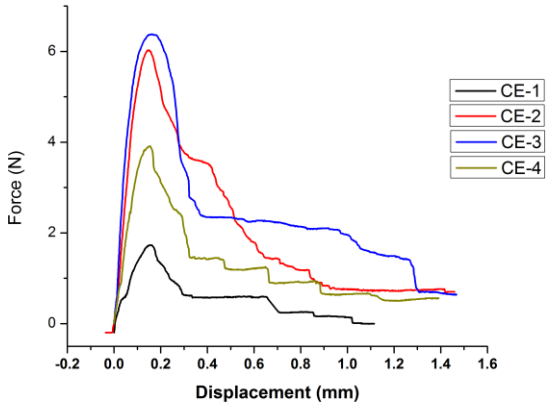

Figure 14. Force displacement curves of ReB_2/PTFE dogbone samples. CE-2 and CE-3 indicate chemical etching of the PTFE surface prior to ReB_2 deposition. CE-4 was sanded prior to deposition, and CE-1 was unmodified.

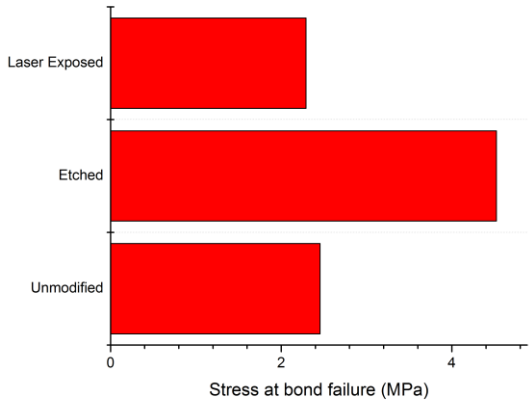

Figure 15. Adhesion failure stress of ReB_2/PTFE

In addition to modulus testing, we wanted to gain an understanding about how strongly the ReB_2 coating adheres to the polymer surface. To accomplish this, we performed a modified pull-off test with a Deben microtester. The PTFE was etched with a special fluoropolymer etchant to increase the binding strength of the adhesive. As a 200 N load is applied to the ReB_2/PTFE sample, a force-strain curve is obtained **(Figure 14)**. The displacement as function of the force applied gives an accurate measurement of the binding strength of the coating to the polymer.[29] The untreated ReB_2 has an average failure stress of 2.5 MPa and does not change if the coating is done on PTFE that has been pre-exposed to the laser. This corroborates the nanoindentation data that shows that the laser did not induce any mechanical change in the polymer. However, if the surface of the PTFE is etched with a fluoropolymer etchant before deposition of ReB_2, the adhesion strength increases by 83% **(Figure 15).** This result could be due to the loss of surface fluorine atoms, which would not enhance surface adhesion. Additionally, image analysis of the samples after pull-off indicates that there are still some areas of ReB_2 deposition on the polymer surface. It is very possible that the pull-off test is only removing the top portion of the coating and the

underlying ReB_2 is unaffected. Successive pull-offs might be necessary to determine the binding affinity of the bottommost layers of ReB_2.

Confined-Plume Chemical Deposition of MnB_2 films using 800-nm pulsed, tabletop, laser irradiation

Using the same multilayer assembly, but switching to the precursor $Mn(CO)_4B_3H_8$, yields films of MnB_2. Although XRD analysis of these films shows the only crystalline product of this deposition to be MnB_2 **(Figure 16)**, the SEM images do not show the same microscale morphology **(Figure 17)** as the ReB_2 films. This observation could be caused by the lower melting point of MnB_2, which is destroying much of the structure of these platelets as they form.

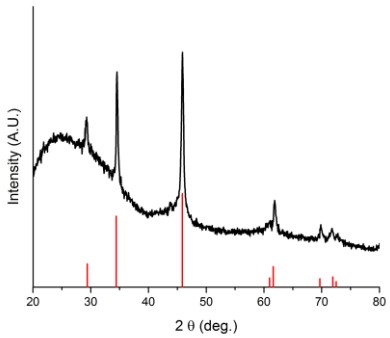

Figure 16. XRD pattern of MnB_2/glass, red drop lines indicate pattern of bulk MnB_2 (PDF#35-0788)

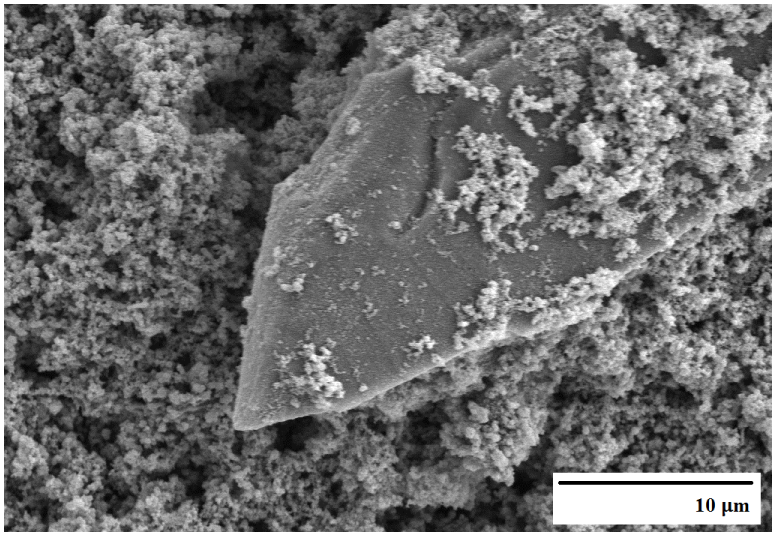

Figure 17. SEM image of MnB_2/glass

Confined-Plume Chemical Deposition of ternary phase $Re_xMn_{(1-x)}B_2$ films using 800-nm pulsed, tabletop, laser irradiation

Recently, it has been shown that ternary alloys of group VI transition metal borides show increased hardness than the representative binary compounds.[30] With this in mind, we sought to create ternary alloys by CPCD. When the molecular precursors, $Re(CO)_4B_3H_8$ and $Mn(CO)_4B_3H_8$ are co-deposited on a glass slide and exposed to femtosecond pulsed 800-nm light, reaction plume formation occurs, and a black deposit is seen on the bottom glass slide. XRD analysis of this film indicates the formation of a solid solution which adopts the ReB_2 crystal structure **(Figure 18)**. Since the covalent radius of manganese (139 pm) is smaller than that of rhenium (151 pm), a contraction of the lattice is seen, shifting the diffraction peaks to higher 2 θ values. Although this structure adopts the ReB_2 unit cell, SEM analysis is more similar to the MnB_2 films, with no platelet structures observed, likely due to a decrease in the melting point of this ternary phase alloy **(Figure 19)**.

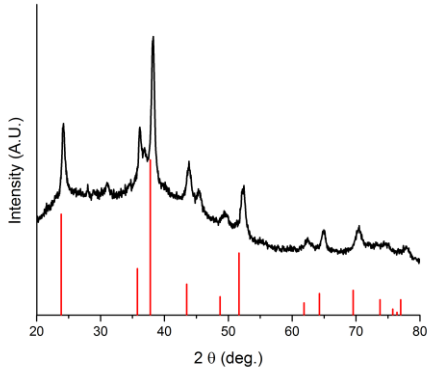

Figure 18. XRD pattern of $Re_xMn_{(1-x)}B_2$/glass

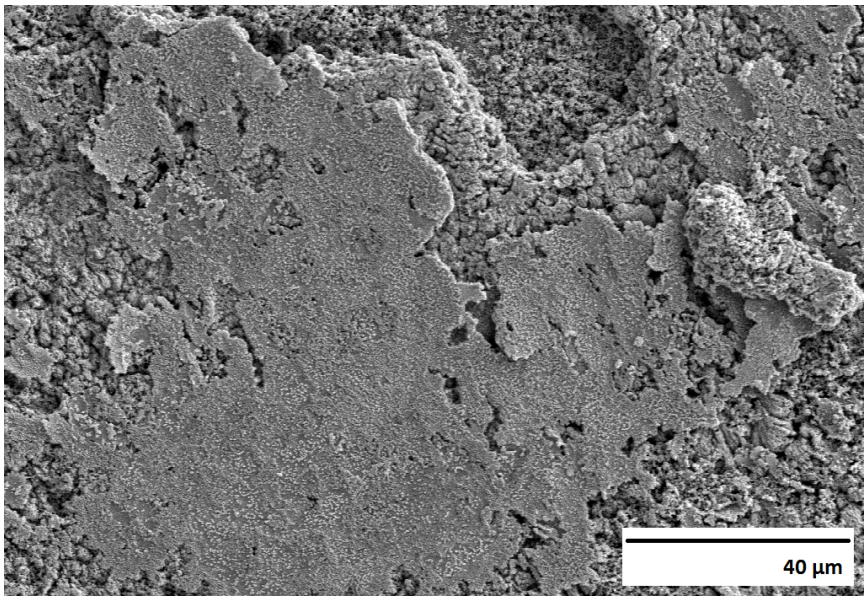

Figure 19. SEM image of $Re_xMn_{(1-x)}B_2$/glass

Confined-Plume Chemical Deposition of ZnO films using 2.94-µm pulsed, tabletop, laser irradiation

In a similar multilayer assembly to the ReB_2 system, ZnO films were deposited on glass substrates from an assembly composed of glass/$Zn_5(OH)_6(CO_3)_2$/glass. Reaction plume formation is evident by a bright white light emanating from the precursor layer **(Figure 20).** After the substrate is scanned through the laser twice, the plume disappears as the precursor has been exhausted. Removal of the top confining glass reveals a dull

white coating on the bottom glass substrate. XRD analysis shows that wurtzite type ZnO is the only crystalline product formed **(Figure 21),** while SEM analysis shows that the film is actually composed of micron-sized particles, and does not form a continuous layer **(Figure 22).**

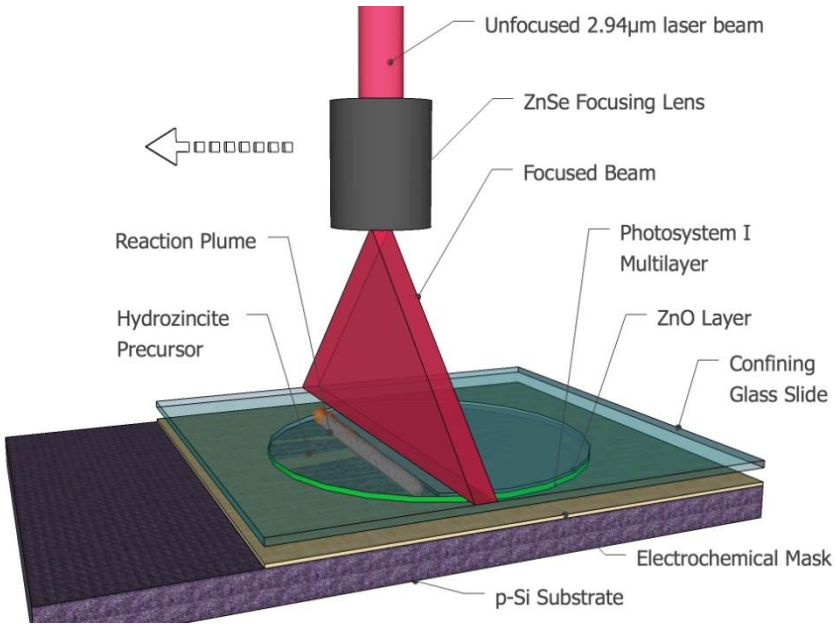

Figure 20. Cartoon depiction of CPCD processing of ZnO films on PSI.

With a rapid process to deposit ZnO films in hand, solid-state photovoltaic device construction can be considered. The conduction band of ZnO lies just below that of the P700 reaction center in photosystem I. This means that ZnO should be a good conductor of electrons that are excited by photon adsorption in a photosystem I layer on p-doped silicon. This electron can then be donated to an anode material such as indium tin oxide, completing a circuit and generating electrical power **(Figure 23)**

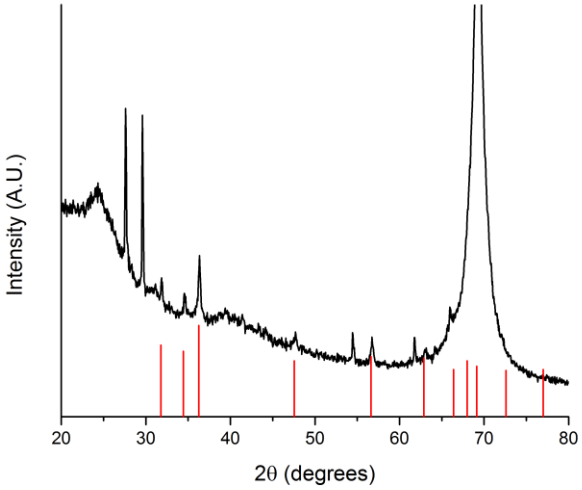

Figure 21. XRD pattern of ZnO/PSI composite. The broad peak and two sharp peaks between 25 and 30° 2 θ are due to the electrochemical mask. The intense peak centered at 70° 2θ is due to the underlying silicon substrate. Red drop line indicate pattern of bulk ZnO (PDF # 36-1451)

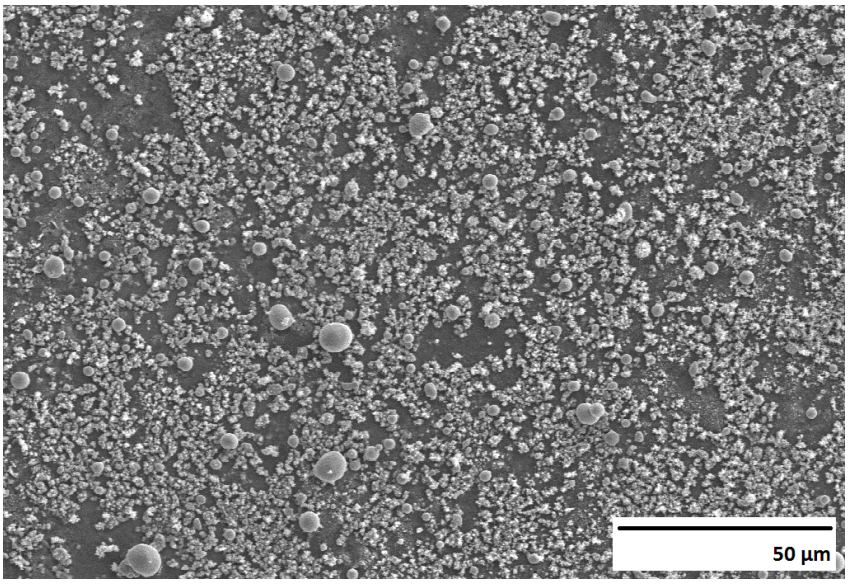

Figure 18. SEM image of ZnO/PSI film.

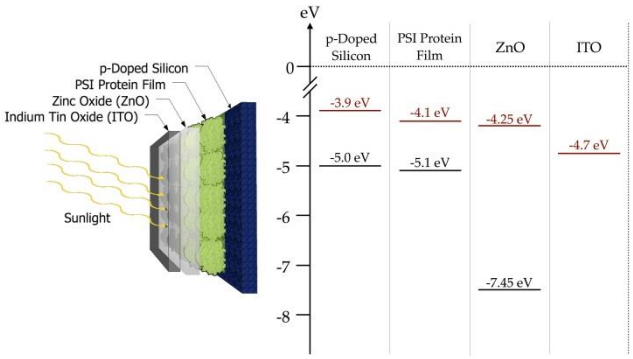

Figure 23. Depiction of band alignment between components of ZnO/PSI solid state device

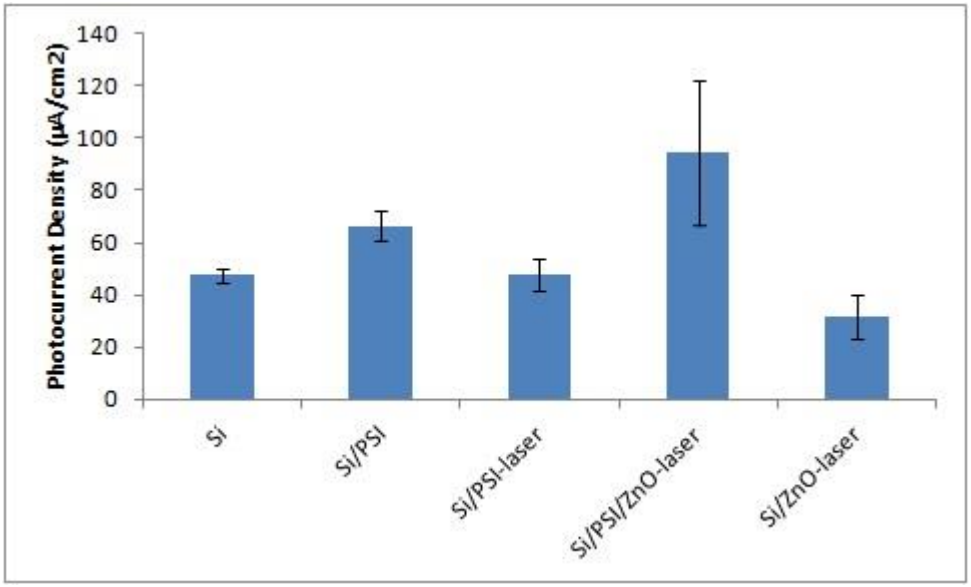

Figure 24. Solid-state photocurrent production of various device architectures.

` To fabricate this device, central experiments are needed to show that the laser irradiation does not damage the photosystem I layer. Exposure of the PSI layer to the infrared laser under the same conditions as during ZnO deposition results in no decrease in photoactivity of the protein. Applying the ZnO precursor to the protein layer, confining it with a glass plate, and scanning it through the laser results in a dull white film of ZnO directly deposited onto the protein surface **(Figure 24).**

The next step in device fabrication is to ensure that the ZnO band has good alignment with PSI to ensure acceptance of electrons from the P700 reaction center. In this experiment, two photochemical mediators, methyl viologen (MV^{2+}) and ruthenium (III) hexammine (RuHex), were used. While both of these mediators are capable of accepting electrons from the P700 reaction center, their band energies are vastly different. Methyl viologen has a band that is only slightly lower in energy than P700, but is higher than that of ZnO, which means it cannot accept electrons from ZnO. The band energy of Ru(Hex) is much lower than that of P700 and ZnO, which indicates it can accept electrons from ZnO. As expected, in a liquid photoelectrochemical cell, the presence of the ZnO layer on PSI blocks almost all electron flow to methyl viologen and greatly increased the photocurrent of the Ru(Hex) system **(Figure 25).**

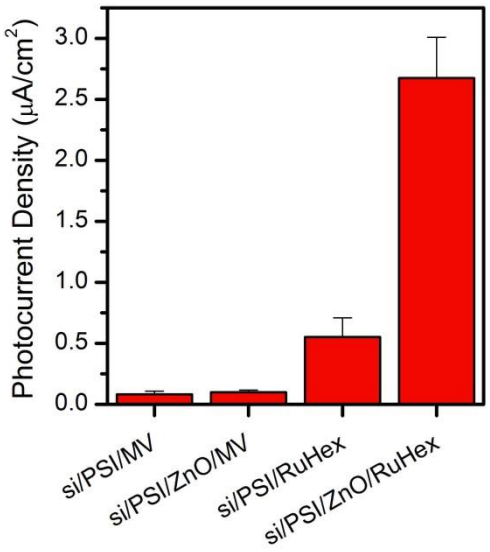

Figure 25. Wet cell photoelectrochemical measurements with MV^{2+} and $Ru(hex)^{2+}$ mediators.

Once the band alignment of the ZnO has been determined, we could then move from a liquid based cell to a solid-state device. A flexible piece of ITO-coated PET was placed over the ZnO film and held in place by a piece of glass and binder clips. The ITO acts as the final electron acceptor in the cell, thereby completing the circuit. Photoelectrochemical measurements were then taken under solar simulation. These measurements showed that a viable solid-state device could be constructed with ZnO deposition occurring on PSI layers. This method has commercial viability as the device manufacturing from start to finish only takes about 5 minutes, allowing for the production of many devices in a short period of time. The resulting device generates a photocurrent of 21 $\mu A/cm^2$ **(Figure 26).** To increase the photocurrent produced, the native insulating SiO_2 layer on the p-doped silicon can be removed by chemical etching, affording a 5-fold increase in photocurrent generation and external efficiency **(Figure 27).** In addition to their high photocurrent production, these devices were tested for their longevity by exposing them to long periods of intense illumination **(Figure 28)** as well as their durability over a period of two weeks **(Figure 29)**. The activity of the device was not affected by long exposure to sunlight. In a practical application, direct exposure to sunlight of periods exceeding 8 hours are expected. Devices with this architecture should be able to perform well under these conditions. The effect of cycling the devices on and off indicates that the device performance drops to a minimum of about 70% of the maximum activity.

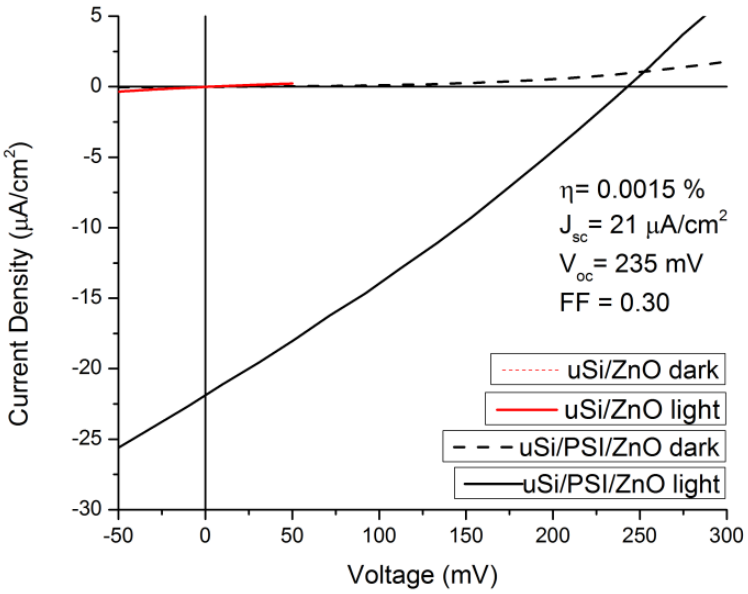

Figure 26. i-V curve of unetched solid-state ZnO/PSI/p-SI device

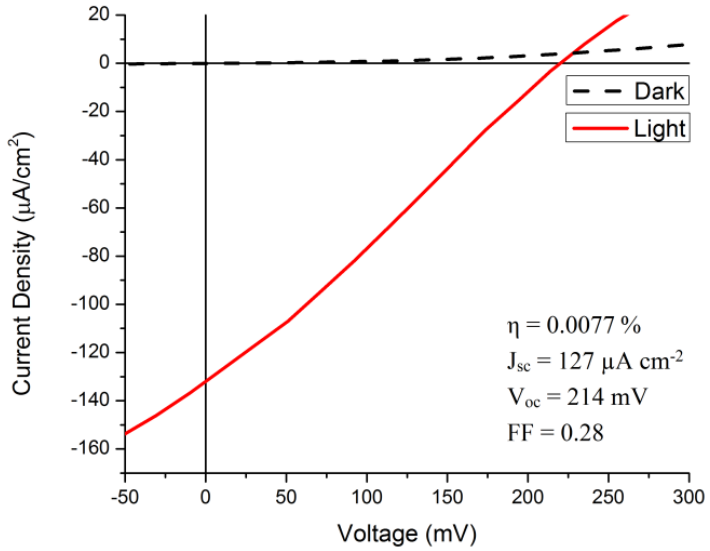

Figure 27. i-V curve of etched solid-state ZnO/PSI/p—Si device

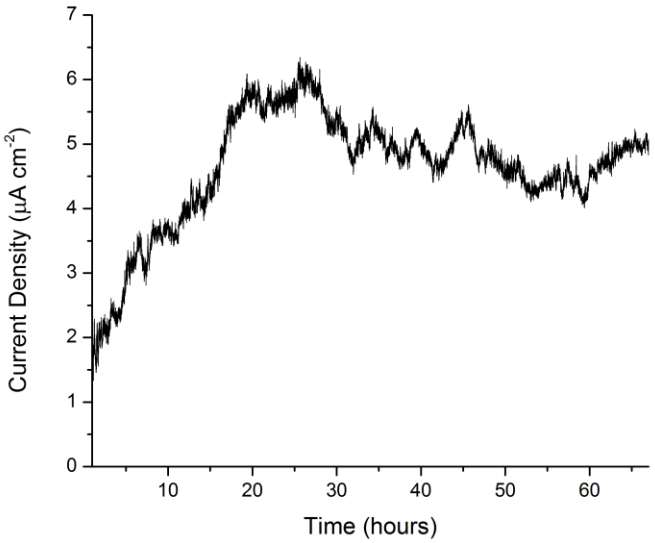

Figure 28. Unetched ZnO/PSI/p-Si device long term exposure to sunlight

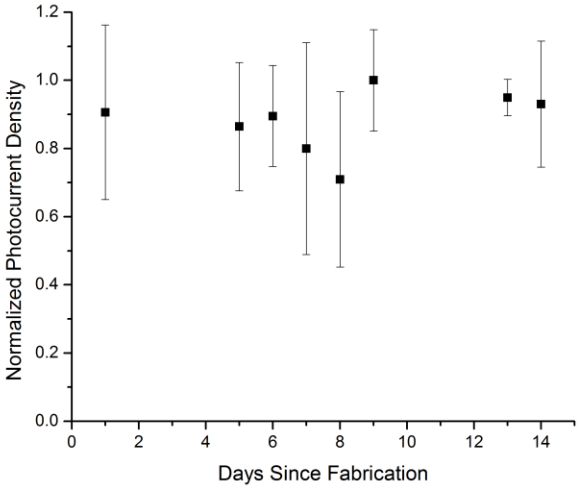

Figure 29. Durability of unetched ZnO/PSI/p-Si devices over a period of two weeks. Devices were tested three times each day.

Confined-Plume Chemical Deposition of CdS films using 800-nm and 2.94-μm pulsed, tabletop, laser irradiation

In addition to ZnO, other semiconducting materials have applications in photovoltaic devices. CdS, a direct band gap semiconductor, has many applications from piezoelectric devices to light emitting quantum dots. When the CdS precursor, cadmium (n-

propyl)dithiocarbamate, is exposed to 2.94-μm light, more rod-like structures are observed. XRD analysis shows CdS as the major crystalline product **(Figure 30).** CdS films were deposited on green onion tissue substrates to further demonstrate the wide variety of substrates CPCD can be performed on **(Figure 31).**

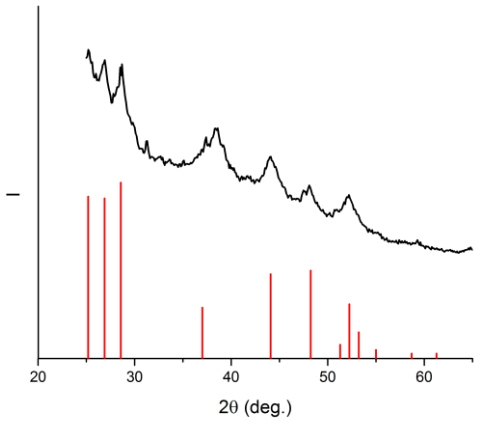

Figure 30. XRD pattern of CdS/onion. Red drop lines indicate bulk CdS (PDF#41-1049).

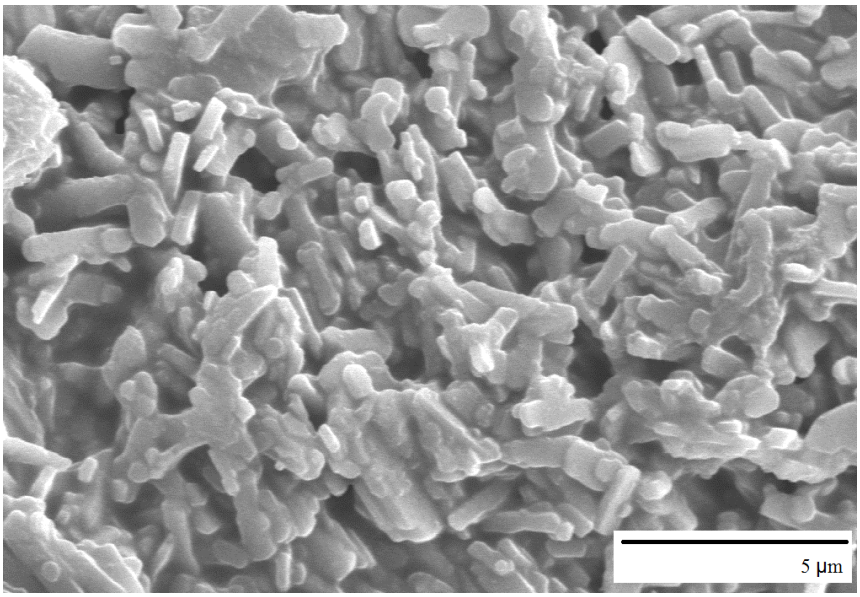

Figure 31. SEM image of CdS/onion

Conclusion

In conclusion, CPCD has successfully been performed using tabletop lasers of three different wavelengths to deposit a variety of materials including ReB_2, MnB_2, ZnO, and CdS. Additionally, ReB_2 has been deposited on ceramic, polymeric, and biological substrates, showing the breadth of this deposition technique. Current studies are underway focused on exploring the adhesion strength of this ReB_2/polymer interface. A solid-state photovoltaic device centered around a ZnO film deposited on a PSI substrate has also been produced.

Chapter II: Synthesis of Binary and Ternary Alloy Nanoparticles for Fuel Cell Applications

Introduction

Heterogeneous Catalysis

The fortuitous discovery of metal catalysis of chemical reactions has paved the way for many important economically relevant industrial processes.[31,32] Catalytic processes can be broken down into two subgroups, homogeneous and heterogeneous. In homogeneous catalysis, both the catalyst and reactant material are in the same state of matter.[33] The bulk of homogeneous catalysis involves the use of discrete molecules with a well-defined mechanism and great selectivity for the chosen reaction. Hydroformylation, the Wacker-Smidt synthesis of acetaldehyde, and some hydrogenations are examples of industrially relevant processes that use homogeneous catalysis.[34,35] In contrast, heterogeneous catalysis has the catalyst and reactant in different states of matter. This is mostly realized with a solid catalyst and a liquid or gaseous reactant. While heterogeneous catalysis has a problem with defined selectivity, the ease of separation of products from the catalyst material allows this process to be used in many industrial processes.[36] Examples of heterogeneous catalyzed reactions include the Haber-Bosch process, the synthesis of sulfuric acid, and the synthesis of ethylene oxide.

Since heterogeneous catalysis is a surface-driven process, bulk metals soon gave way to metal nanoparticles which have a higher surface area to volume ratio. This means that the specific reactivity of a nanoparticle based catalyst would be higher than an equivalent mass of the bulk metal. This trend of increasing surface area led to the development of 2-D rafts and even catalysts consisting of single metal atoms.

While the use of nanoparticles increases the specific reactivity of the catalyst, single component catalysts can be poisoned by intermediate species. One good example of this effect is seen in the oxidation of short chain alcohols and carboxylic acids, such as methanol and formic acid by platinum metal.[37,38] Carbon monoxide can form during the incomplete oxidation of these fuels and binds strongly to the platinum surface.[38] This can be alleviated by increasing the electrical potential or temperature of the catalyst but results in a loss of energy efficiency. It can also be alleviated by the addition of an oxophilic metal in close proximity to the platinum, such as tin or lead.[31,39–42] These metals will adsorb oxygen species which allow a low-energy pathway for the carbon monoxide adsorbed on the platinum atoms to leave as carbon dioxide and reopen the surface for further catalysis. The incorporation of these metals can be accomplished by introducing adsorbed atoms onto the surface, but the distribution of atoms is hard to control.[43] A more controlled method of incorporating these metals is by the synthesis of a binary alloy.

Polymer Electrolyte Membrane Fuel Cells

The complete oxidation of many small organic acids and alcohols is an interesting avenue for alternative energy generation. The energy density of many of these molecules is lower than that of petroleum; however, they can be considered renewable sources of energy as we derive them from biological sources such as corn and sugarcane. Methanol has been studied extensively as an alternative fuel source. Its direct oxidation pathway is as follows:

$$CH_3OH + \frac{1}{2}O_2 \rightarrow CO_2 + 4\,H^+ + 4e^-$$

While methanol can be oxidized by a number of materials, it has drawbacks that prevent it from being used in many commercial applications. Among these drawbacks is the ability for it to cross over the membrane separating the anode and cathode in a fuel cell. The membrane materials are charged to conduct protons across them, but a molecule like methanol, which is neutral at almost all relevant pH values (pKa =15.7), can cross over through the membrane.[38] Once it crosses this membrane, it can be reduced at the cathode and poison the catalyst surface. A better fuel would be one that is charged under operating conditions so that crossover is not an issue.

Formic acid is another small organic molecule that meets this requirement. Its pKa is 3.75, which means it is mostly deprotonated under normal operating conditions.[44,45] Additionally, formic acid can typically be used in higher concentrations than other fuels, greatly increasing its power density. One downside of formic acid is that it freezes at 4 °C, making it not practical to use in certain situations. Additionally, it has two oxidation pathways that can be utilized. The direct pathway is the preferred pathway for optimal operation in a fuel cell:

$$HCOOH \rightarrow CO_2 + 2H^+ + 2e^-$$

Unfortunately, it has an indirect pathway for oxidation as well:

$$HCOOH \rightarrow CO + H_2O$$

$$H_2O \rightarrow OH_{ads} + H^+ + e^-$$

$$OH_{ads} + CO \rightarrow CO_2 + H^+ + e^-$$

This indirect pathway requires two metals in close proximity to be able to remove the CO intermediate which prevents the catalytic process from proceeding. Platinum, an otherwise great catalyst for formic acid oxidation, is especially prone to being poisoned by CO due to strong surface adsorption. To prevent this indirect pathway from dominating the catalytic process, another metal can be alloyed with platinum that allows the direct pathway to proceed, or to lower the activation energy needed to remove the CO from the platinum surface. Lead is a good candidate for alloying with platinum as it is very inexpensive and forms stable phases with platinum.

At the cathode of these fuel cells, oxygen is reduced to water through the use of another catalyst. Again, while platinum is one of the most active catalysts to perform this reaction, its cost prohibits it for being used in a widespread commercial application. To alleviate costs of this cathode catalyst, alloys of early period transition metals with carbon, oxygen and nitrogen are currently being researched. The ability to tune band energy of these metals to activate the O-O bond in oxygen makes them attractive choices for oxygen reduction catalysts. In other cell designs, this catalyst at the cathode can just be used to form hydrogen from the protons produced at the anode. Bimetallic alloys of platinum and other precious metals are the best performing catalysts for this application.

Experimental Methods

Synthesis of PdAu/GCNF

K_2PdCl_4 and $HAuCl_4$ (see **Table 1** for specific details) were added to 1.5 L deionized water (18.2 MΩ) and stirred under a N_2 atmosphere for 90 minutes. Meanwhile, 25 mg of graphitic carbon nanofibers (GCNF) were suspended by sonication in 5 mL methanol and added to the salt solution and stirred for 2 hours. Then, $NaBH_4$ (see Table 1) was added to

the solution dropwise over 10 minutes and stirred for an additional hour. The solution was then filtered through Whatman Anodisc 47 filter paper and a black alloy composite, Pd_xAu_y/GCNF, was collected.

Table 1. Synthetic parameters for the synthesis of Pd_xAu_y/GCNF alloys by solution metal ion reduction

Sample ID	Mass K_2PdCl_4	Mass $HAuCl_4$	Mass $NaBH_4$
JCB-1-40	26.9 mg (0.08 mmol)	28 mg (0.08 mmol)	31 mg (0.80 mmol)
JCB-2-40	39.8 mg (0.12 mmol)	20.7 mg (0.06 mmol)	35 mg (0.93 mmol)
JCB-1-37	26.8 mg (0.08 mmol)	28 mg (0.08 mmol)	35 mg (0.93 mmol)
JCB-1-41	108 mg (0.33 mmol)	28 mg (0.08 mmol)	156 mg (4.0 mmol)
JCB-3-41	163 mg (0.50 mmol)	33.9 mg (0.10 mmol)	56.6 mg (1.5 mmol)
JCB-4-41	163 mg (0.50 mmol)	67.9 mg (0.20 mmol)	47 mg (1.2 mmol)
JCB-5-41	159 mg (0.48 mmol)	207 mg (0.60 mmol)	103 mg (2.7 mmol)

Synthesis of TaO_x nanoparticles by sol-gel[46]

50 mL cyclohexane, 0.456 mL i-butanol, 0.623 mL deionized water, and 1.50 mL Igepal CO-630 were added to a 250-mL round-bottom flask and let stir for 2 hours. Then, 1 mL $Ta(OEt)_5$ was added and the solution became turbid after 5 minutes. The solution was stirred an additional 2 days and most of the solvent was removed by rotary evaporation and 50 mL ethanol was added. The solution was stirred an additional hour then centrifuged; a gel was collected and dried in air overnight. A portion of the powder was reduced under 10% H_2/ 90% N_2 at 800 °C for 1 hour. Catalyst samples were characterized by TEM, XRD, and various electrochemical techniques.

Synthesis of TaO_x and TaO_xN_y catalysts

The gel from the previous synthesos was suspended in 5 mL ethanol and dropcast onto silicon wafers and dried to create a thin film of particles. These films were then heated under a 50% argon/50% hydrogen atmosphere to temperatures ranging from 500-800 °C for 1 hour. Attempts to incorporate nitrogen into the structure were accomplished by treatment with ammonia instead of argon/hydrogen. After cooling, the now black particles were scraped from the silicon wafers and characterized by TEM, XRD, and various electrochemical techniques.

Synthesis of PtPb/C by solution metal ion reduction[40]

$H_2PtCl_6{\cdot}6H_2O$ or K_2PtI_6 and $Pb(OAc)_2{\cdot}3H_2O$ are codissolved in 1 L degassed methanol under a nitrogen atmosphere and stirred for 1 hour. Then, 25 mg carbon support material is added to the salt solution and stirred an additional hour. A large excess of $NaBH_4$ is dissolved in 15 mL degassed methanol and quickly added to the salt solution. After stirring overnight, the solution is filtered through Whatman Anodisc 47 filter paper, and a black composite was collected. This material is characterized by TEM, XRD, TGA, ICP-OES, and various electrochemical techniques.

Synthesis of $[Pt(Me)_2(SEt_2)]_2$[47]

In a three-neck round bottom flask equipped with a magnetic stirring bar under a nitrogen atmosphere, $PtCl_2(SEt_2)_2$ is dissolved in 15 mL of dry, distilled benzene and cooled to 0 °C. Then, a 2 M solution of methyllithium in diethylether is added dropwise as the color of the solution changes from yellow to white. The solution is stirred for 1.5 hours, then quenched with a small amount of chilled deionized water. The solution is then extracted with portions of dichloromethane and the organic fractions are collected and dried. The

resulting white solid is then recrystallized from benzene and dichloromethane to yield white crystals of $[Pt(Me)_2(SEt_2)]_2$.

Synthesis of $Pt(Me)_2(bpy)$

In a three neck round bottom flask equipped with a magnetic stirring bar under a nitrogen atmosphere, $[Pt(Me)_2(SEt_2)]_2$ is dissolved in dry, distilled benzene, and heated to 60 °C. Then, solid 2,2-bipyridyl (bpy) is added to the solution which results in an immediate color change to dark red. The solution is stirred for 5 minutes, then the solvent is removed by rotary evaporation to yield $Pt(Me)_2(bpy)$.

Synthesis of $Pt(Me)_2(bpy)(PbPh_2Cl)(Cl)$[48]

In a three neck round bottom flask equipped with a magnetic stirring bar under a nitrogen atmosphere, $Pt(Me)_2(bpy)$ is dissolved in dry tetrahydrofuran. This solution must have exposure to natural sunlight. Then, solid dichlorodiphenyllead is added and the solution turns from orange to yellow over the course of five minutes. The solvent is removed by rotary evaporation and the product is recrystallized from dichloromethane and benzene to yield yellow crystals of $Pt(Me)_2(bpy)(PbPh_2Cl)(Cl)$.

Synthesis of $Pt(Me)_2(Ph_2Me_2Phen)$

In a three neck round bottom flask equipped with a magnetic stirring bar under a nitrogen atmosphere, $[Pt(Me)_2(SEt_2)]_2$ is dissolved in dry, distilled benzene, and heated to 60 °C. Then, solid 2,9-dimethyl-4,7-diphenyl-1,10-phenanthroline (Ph_2Me_2Phen) is added to the solution which results in an immediate color change to orange. The solution is stirred for 5 minutes, then the solvent is removed by rotary evaporation to yield $Pt(Me)_2(Ph_2Me_2Phen)$.

Synthesis of $Pt(Me)_2(Ph_2Me_2Phen)(PbPh_2Cl)(Cl)$

In a three neck round bottom flask equipped with a magnetic stirring bar under a nitrogen atmosphere, $Pt(Me)_2(Ph_2Me_2Phen)$ is dissolved in dry tetrahydrofuran. This solution must have exposure to natural sunlight. Then, solid dichlorodiphenyllead is added and the solution turns from orange to yellow over the course of five minutes. The solvent is removed by rotary evaporation and the product is recrystallized from dichloromethane and benzene to yield yellow crystals of $Pt(Me)_2(Ph_2Me_2Phen)(PbPh_2Cl)(Cl)$.

Synthesis of PbPt/C from single-source precursors $Pt(Me)_2(Ph_2Me_2Phen)(PbPh_2Cl)(Cl)$

The single-source precursors are dissolved in 15 mL chloroform and stirred for 30 minutes. Then, 25 mg of carbon support material are added to the solution and stirred an additional 30 minutes. The solvent is removed under vacuum, and the black composite is resuspended in 5 mL pentane by sonication. The black suspension is then dropcast onto silicon wafers and dried. The silicon wafers are placed in a tube furnace under a 10% hydrogen/90% nitrogen atmosphere and heated to 550 °C and held for 1 hour. After cooling, the composite powders are scraped from the silicon wafers and characterized by XRD, TEM, TGA, ICP-OES, and various electrochemical techniques.

Electrochemical Analysis of PbPt/C samples

Catalyst inks are prepared by suspending 5 mg catalyst nanocomposite in 4 mL DI water, 1 mL isopropanol, and 50 µL Nafion. This suspension is sonicated for 10 minutes, and a 10 µL drop is placed directly on a freshly cleaned and polished glassy carbon working electrode and dried. Cyclic voltammograms are collected on a CHI660A potentiostat in either 0.5 M H_2SO_4 or $HClO_4$ with a platinum counter electrode and an Ag/AgCl (3 M KCl) reference electrode. Electrochemical surface area is determined by hydrogen absorption

onto platinum, or by carbon monoxide stripping. Carbon monoxide is bubbled into the acidic solution for 10 minutes while the working electrode is held at 0.1 V (vs. Ag/AgCl). The electrode is then scanned from 0.1 – 1.0 V and the peak area is determined to calculate the surface area of Pt sites on the catalyst.

Additional cyclic voltammograms are collected in solutions containing 0.5 M HCOOH in 0.1 M H_2SO_4. Rotating disk electrode i-t curves are collected at 1000 rpm in solutions of either 0.5 M or 10 MHCOOH in 0.1 M H_2SO_4 over a period of 10 minutes.

Results and Discussion

PdAu/GCNF Composite Catalysts

At the cathode of a proton exchange membrane fuel cell, the protons that have crossed the electrolyte membrane are reduced to hydrogen. Typically, platinum has been one of the highest performing catalysts for hydrogen production, but it is expensive. To lower the cost of platinum based catalysts, platinum can be alloyed with a base metal which can increase the overall activity while decreasing the cost. Alternatively, less expensive metals can be alloyed together to achieve activities close to or exceeding that of platinum.

When synthesizing nanoparticle alloys, it is quite common to use surfactants to help control particle size and morphology; however, when these nanoparticles are to be used for catalytic processes, this surfactant can interfere and retard the catalytic pathway. Developing synthesis strategies that can form nanoparticles without the use of surfactants is important for the catalysis field.

The palladium-gold binary system does not have any ordered alloys that are stable at room temperature. Instead, when these two metals are alloyed, they form a solid

solution. In a solid solution, the atom are randomly distributed throughout the unit cell. Since both palladium and gold adopt a face centered cubic unit cell, so too does the solid solution. Palladium and gold have different atomic radii, 137 and 144 pm respectively, so the amount of each metal in an alloy can be determined by the x-ray diffraction pattern using Vegard's law,

$$a_{A_{(1-x)}B_x}=(1-x)a_A+xa_B$$

where a_A is the d-spacing of constituent A, a_B is the d-spacing of constituent B and x is the atomic percent of constituent B. Vegard's law states that the d-spacing of a solid solution reflection is a weighted average of the constituent atom d-spacing of the same reflection.

A number of alloy compositions along the solid solution of $Pd_{1-x}Au_x$/GCNF were synthesized by the solution metal ion reduction of K_2PdCl_4 and $HAuCl_4$ in water by sodium borohydride followed by the addition of GCNF support and subsequent filtration. XRD analysis of these nanocomposites shows that the PdAu alloy is the only crystalline product formed **(Figure 1).** From the broad peaks seen in the diffraction pattern, the average particle size can be calculated from the Scherrer equation:

$$\tau = \frac{k\lambda}{\beta \cos\theta}$$

where the particle size in angstroms (τ) is dependent on the angle of the reflection (θ), full width at half max of the peak (β), as well as the wavelength of the x-ray source (λ) and a structure factor (k) dependent on the particle shape, which for spherical particles is 0.9. As particle size decreases, the number of unit cells in the crystal also decreases. When the number of unit cells is small enough, diffracted x-rays that do not obey Bragg's law do not

have another x-ray completely out of phase to cause destructive interference. Therefore instead of seeing zero intensity where Bragg's law is not met, only a slight reduction in the intensity is observed. On a diffraction pattern, this is observed as broad peaks. Other factors that can influence the determination of particle size include the shape of the particles, intraparticle strain, as well as instrumental broadening. TEM analysis of these alloys show spherical nanoparticles well dispersed across the carbon surfaces **(Figures 2-9).** A summary of particle sizes is seen in **Table 2.**

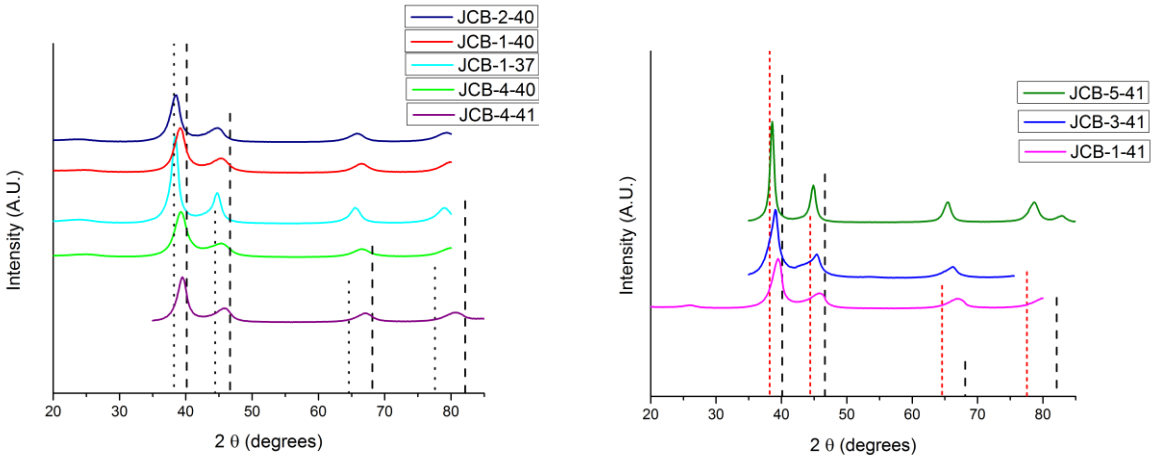

Figure 1. XRD patterns of various PdAu/C stoichiometries. Dashed lines indicate the pattern of bulk palladium (PDF#46-1043), while dotted lines indicate the pattern of gold (PDF#04-784)

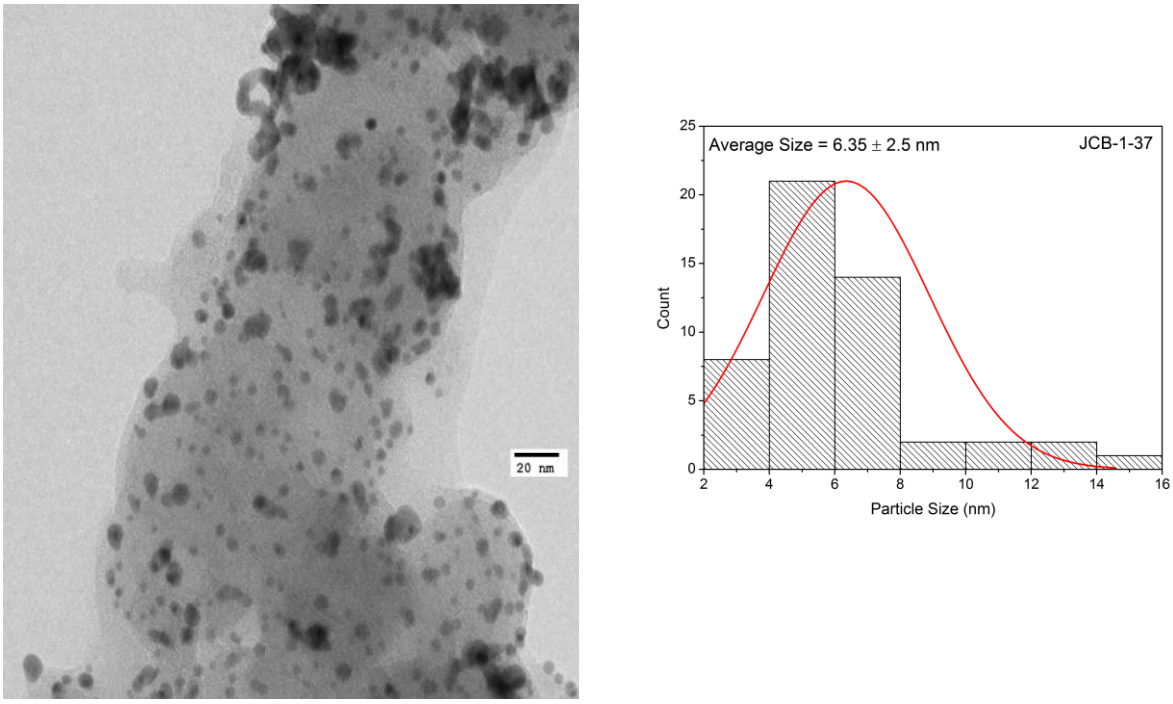

Figure 2. TEM image of JCB-1-37

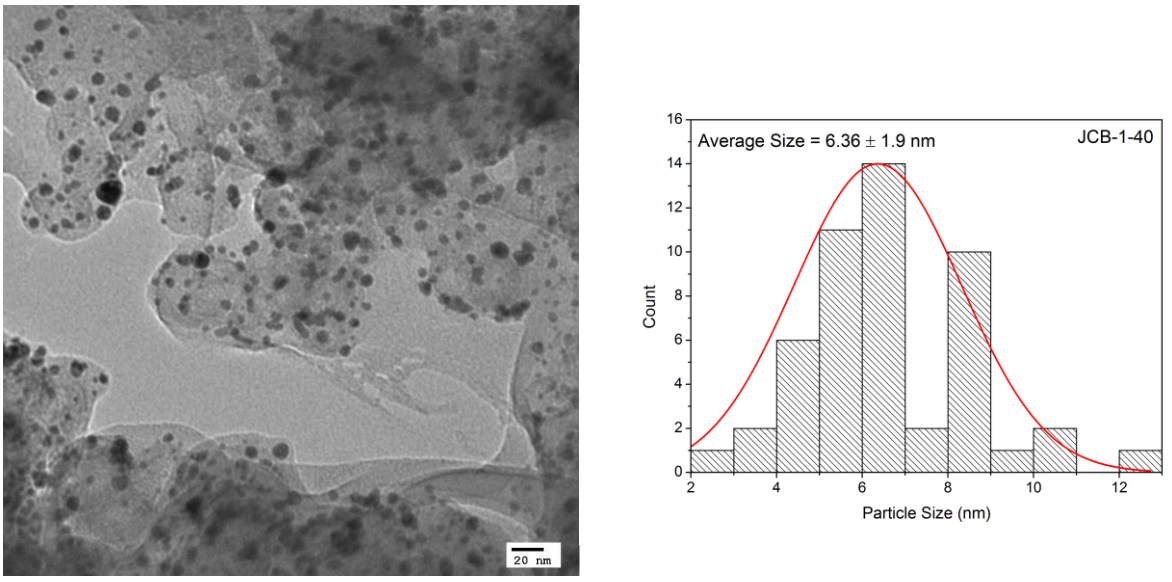

Figure 3. TEM image of JCB-1-40

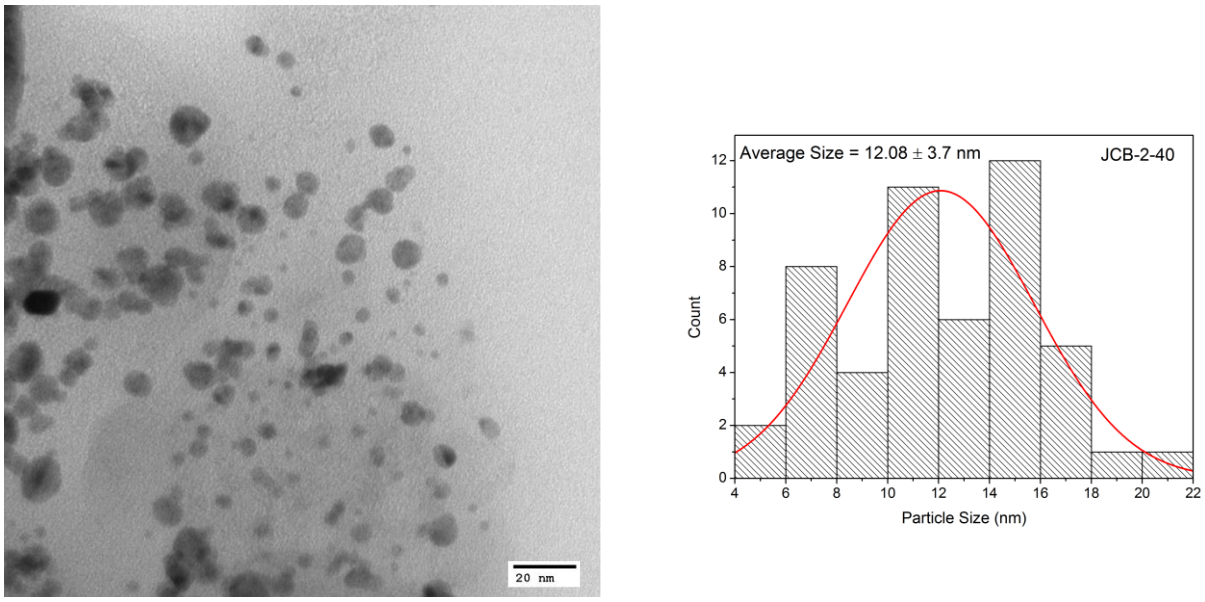

Figure 4. TEM image of JCB-2-40

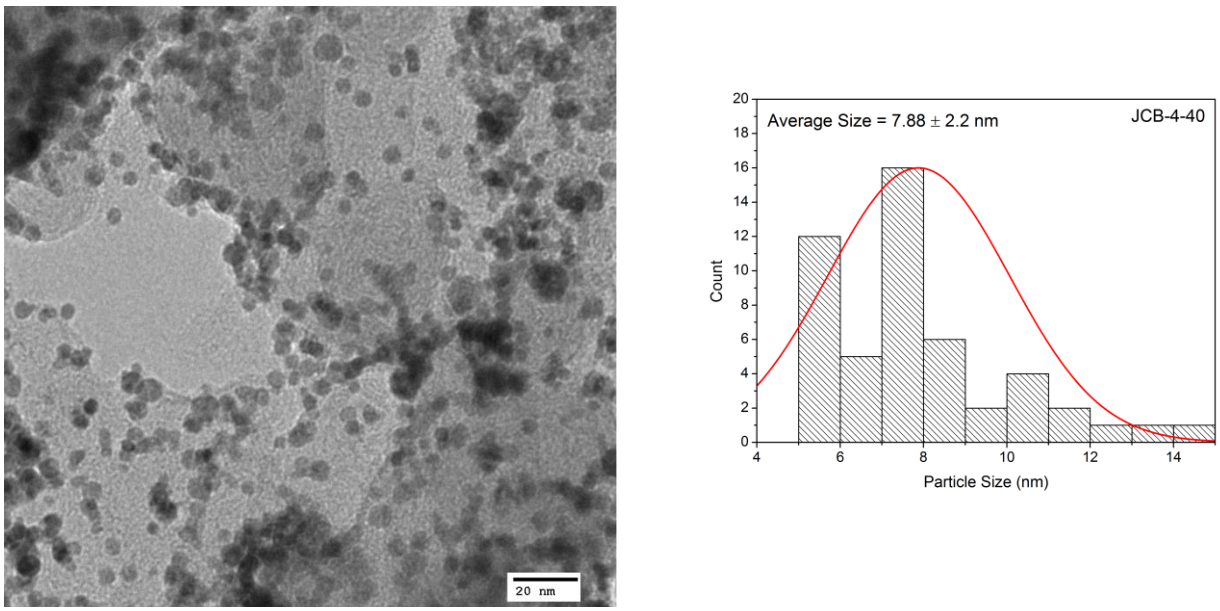

Figure 5. TEM image of JCB-4-40

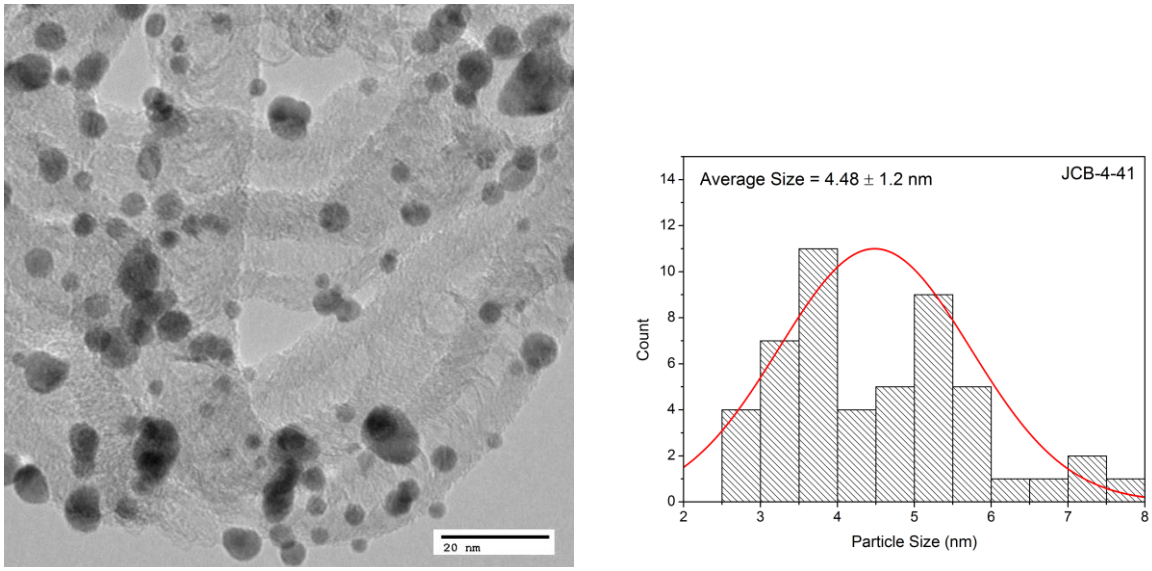

Figure 6. TEM image of JCB-4-41

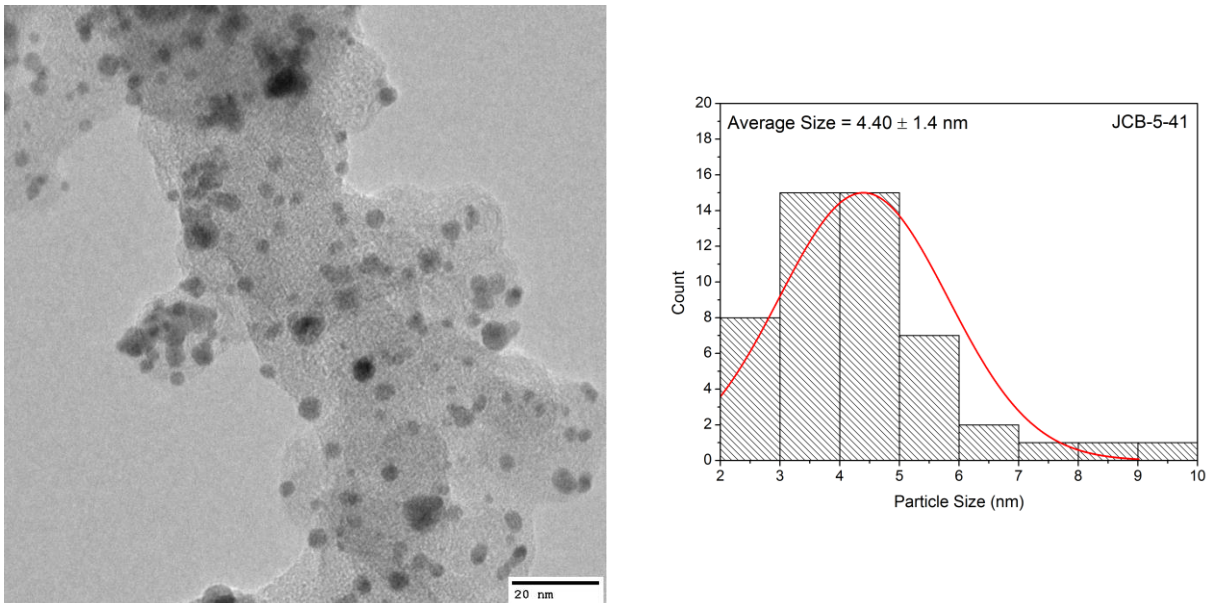

Figure 7. TEM image of JCB-5-41

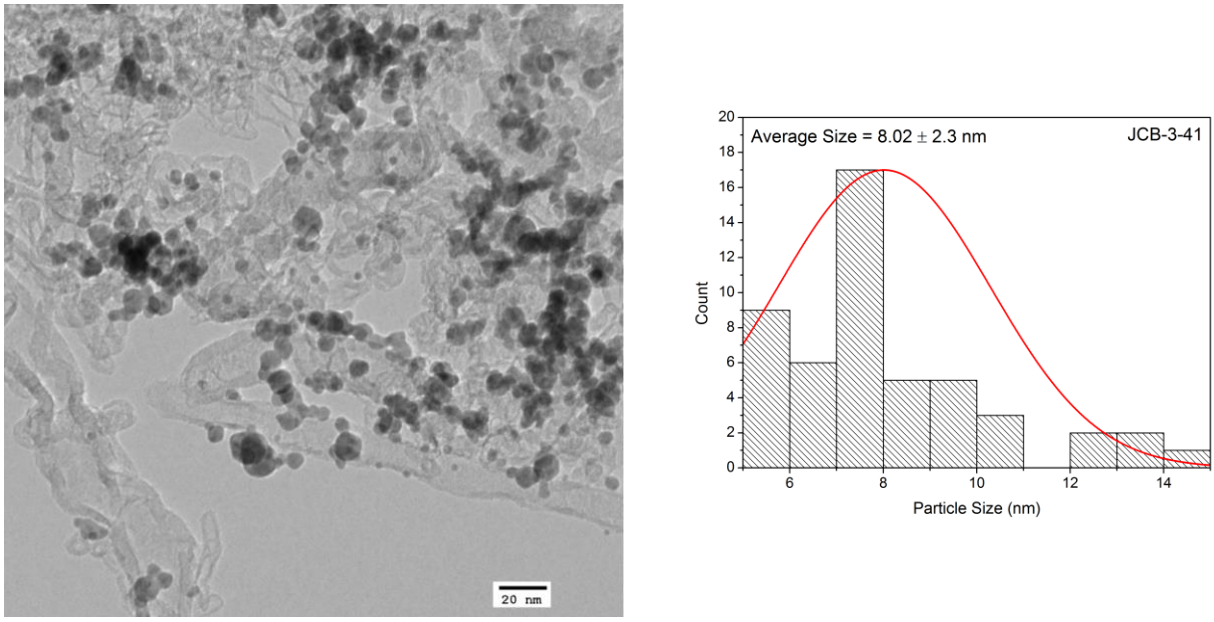

Figure 8. TEM image of JCB-3-41

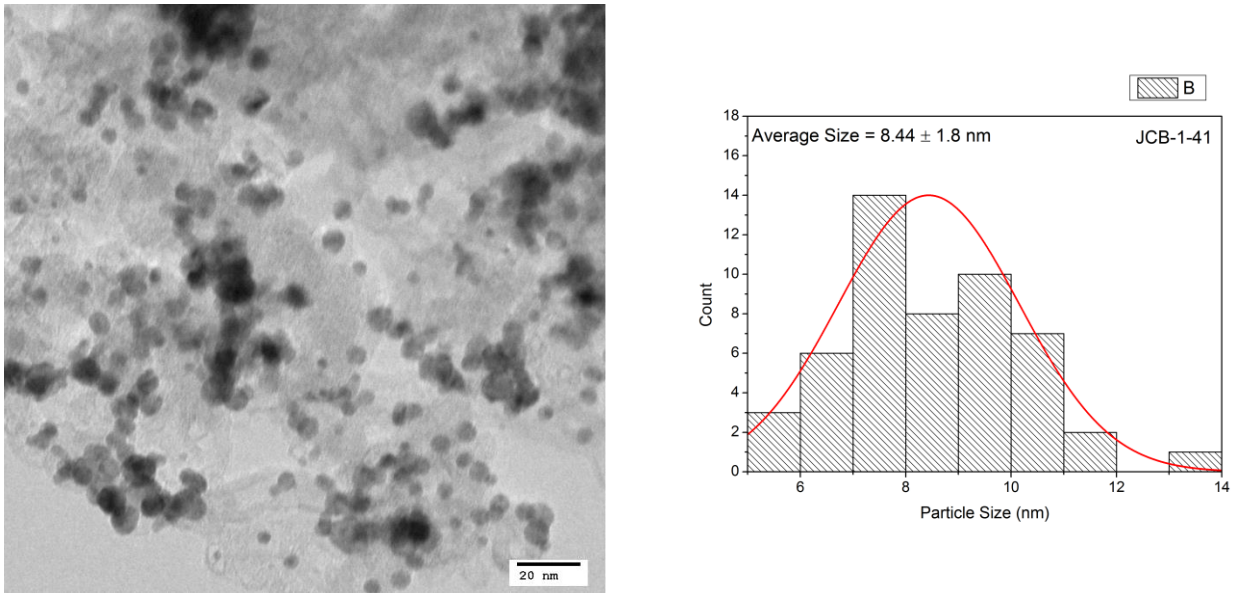

Figure 9. TEM image of JCB-1-41

Table 2. Summary of stoichiometry and particle size of each PdAu/C alloy composite.

Sample	Molar ratio Au:Pd	Scherrer's Analysis Particle size (nm)	Histogram particle size (nm)
JCB-1-37	1.78	_	6.35 ± 2.5
jCB-1-40	3.39	14.9 ± 2	6.36 ± 1.9
JCB-2-40	2.31	6.18 ± 1.2	12.08 ± 3.7
JCB-4-40	0.85	8.00 ± 1.8	7.88 ± 2.2
JCB-4-41	2.67	14.7 ± 3	4.48 ± 1.2
JCB-5-41	0.38	6.07 ± 1.3	4.40 ± 1.4
JCB-3-41	1.00	8.47 ± 1.4	8.02 ± 2.3
JCB-1-41	0.51	8.20 ± 1.5	8.44 ± 1.8

Electrochemical Analysis of PdAu/C

Cyclic voltammetry is a widely used electrochemical technique that is useful for measuring the consumption of an analyte in solution. In a typical three-electrode set-up, current is measured at the working electrode, where oxidations and reductions are taking place in comparison to a voltage applied against a reference electrode.

For the PdAu system, the composite powders are sonicated in a mixture of water, isopropanol and Nafion to create a catalyst ink which is applied directly onto the surface of a glassy carbon electrode. This ink mixture allows the catalyst to remain in good electrical contact with the surface and not wash off during the experiment. Since we are interested in the hydrogen evolution of these catalyst materials, the analyte in this case is sulfuric acid.

Cyclic voltammograms of PdAu/C alloys in general show two distinct features. First, is the evidence of hydrogen evolution at palladium atoms seen right around 0 V (vs. vg/AgCl), the second feature is seen around 0.55 V (vs. Ag/AgCl) which is reduction of surface palladium atoms.

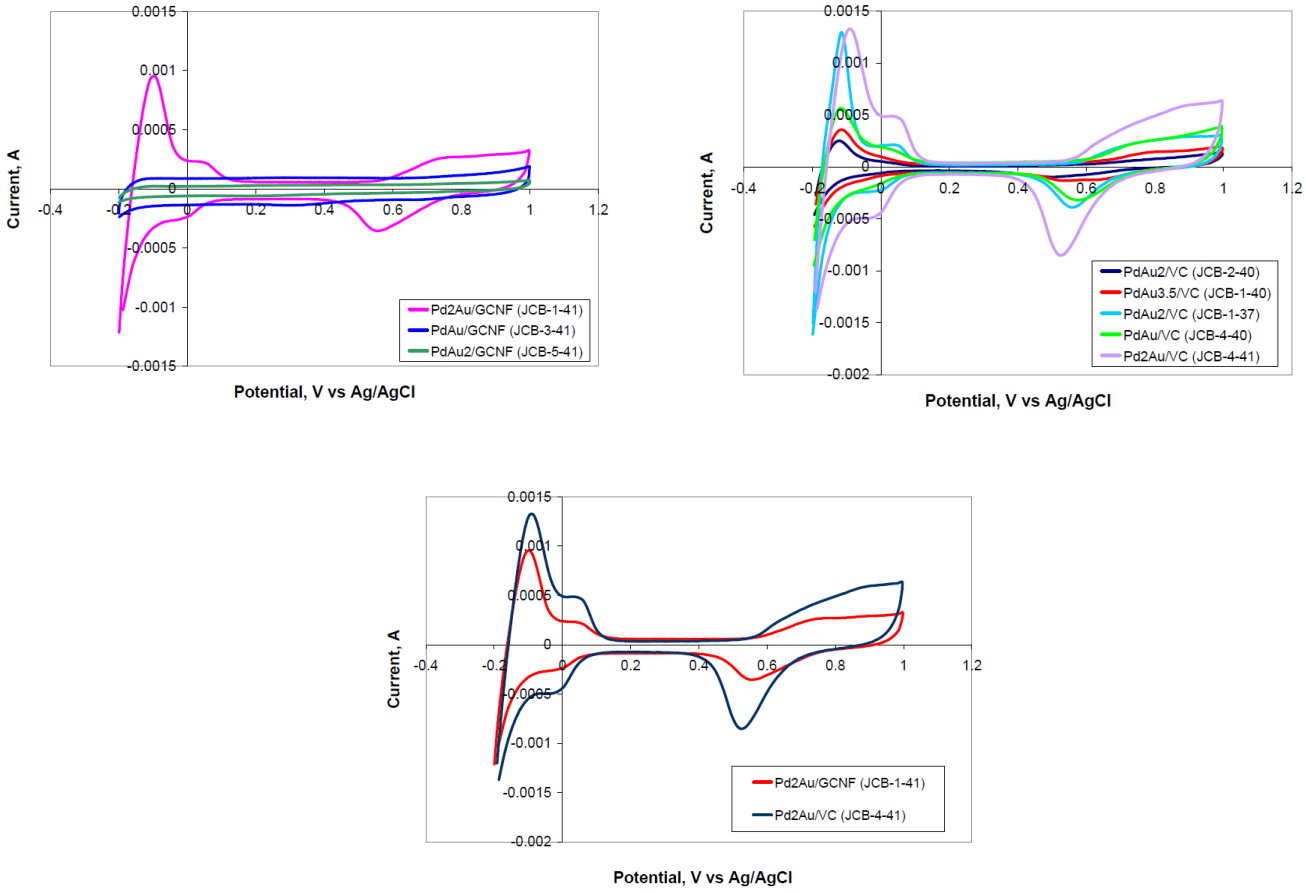

Figure 10. CV scans of PdAu/C catalysts

From the CV studies, JCB-4-41 and JCB-1-41 were the most active catalysts for hydrogen evolution, but there is no correlation between the stoichiometry of these alloys and their performance. Additionally, since particle size was uniform across all samples, the surface area of the catalysts should not factor into the performance issues **(Figure 10).**

Tantalum-based catalysts

Sol-gel chemistry can be used to make nanoparticles of many metal oxides. In sol-gel processing, a metal alkoxide is dissolved in an organic solvent with a long chain surfactant that will create micelles.. Since the alkoxides are soluble in both organic and aqueous solvents, they can travel into and out of the micelles the surfactant forms.[49] A small amount of water is then added, along with an acidic or basic catalyst, and the alkoxide slowly hydrolyzes to create a metal oxide network inside of the micelle. After washing and centrifugation, a gel of the metal oxide network can be obtained.

At the cathode in a fuel cell, oxygen is usually reduced to water using platinum metal catalysts. However, platinum is expensive and cheaper materials are sought to perform this process. Early transition metal alloys of oxygen, nitrogen and carbon have been studied for the oxygen reduction reaction as they have partially filled d-orbitals that can activate O_2.

For the synthesis of TaO_x gels, tantalum (v) ethoxide was hydrolyzed in the presence of ammonium hydroxide in cyclohexane. The slow hydrolysis was evident as the solution became opaque over the course of two days. Once isolated, the sample was divided into two parts, one was heated under a reducing atmosphere (Figure X) and an attempt was made to incorporate nitrogen into the gel by treatment with ammonia at elevated temperatures. This resulted in the formation of tantalum nitride **(Figure 11).** XRD analysis of the reducing atmosphere treated sample shows the only phase present to be {Ta O}, which is a suboxide between the phases of TaO_2 and Ta_2O_5, which indicates that there are some partially filled d-orbitals in this sample. The ammonia treated powder has completely converted to Ta_3N_5, which is a d^0 material. Attempts to perform oxygen reduction with

these catalysts were unsuccessful, as the materials had no ORR activity. Single-source precursor design is a challenging step in the development of an alloy by thermal reduction. Not only does the molecule need to contain both metal species, the extraneous ligands must not decompose to form stable phases with these metals. While there are many molecules that contain a lead platinum bond, a large majority of these molecules contain phosphine ligands, which will thermally decompose to form Pt-P phases. To remove the possibility of this impurity forming, substitutions from phosphine ligands to nitrogen based ligands, such as bipyridine and anthracene derivatives were chosen, as there are no known stable Pt-N or Pb-N phases.

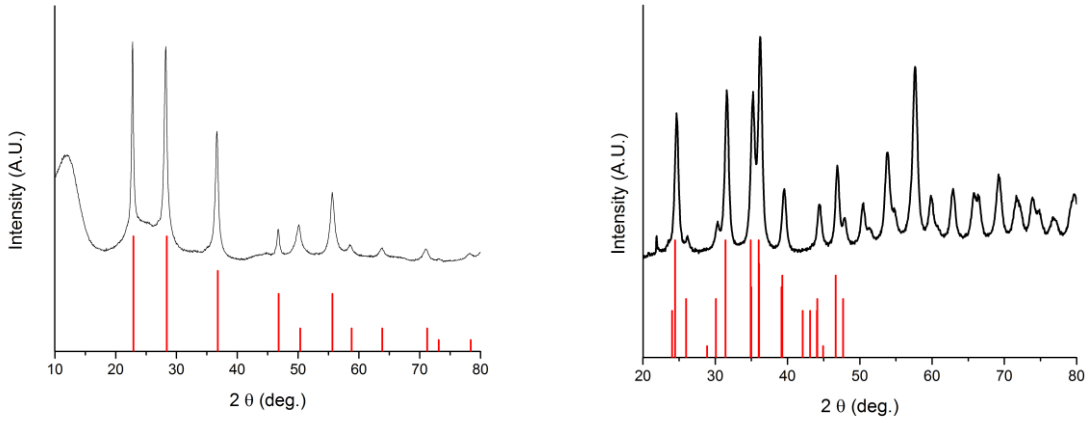

Figure 11. (left) XRD pattern of TaO_x sol-gel heat treated at 800 °C under 10% H_2. Red lines indicate bulk {Ta O} (PDF#19-1299). (right) XRD pattern of TaO_x sol-gel treated with ammonia at 800 °C. Red lines indicate bulk Ta_3N_5 (PDF#19-1291)

PtPb/C Composite Catalysts

Carbon supported bimetallic alloys of platinum and lead were synthesized by two methods. The first method, solution-metal ion reduction, is accomplished by the reduction of a methanolic solution of lead and platinum salts. The lead-platinum phase diagram shows that there are three stable alloy compositions, Pt_1Pb_1, Pt_3Pb_1 and Pt_1Pb_4. Therefore

the stoichiometry of the precursor salts is very important to ensure the successful synthesis of the desired composition. Due to the large difference in reduction potentials of these metals (Pt^{2+}->Pt^{0} 1.18 V vs. SHE, Pb^{2+}->Pb^{0} -0.12 V vs. SHE), it is thought that reduction of these metal ions would result in reduction of platinum, followed by reduction of lead to achieve nanoparticles of both metals. To ensure co-reduction into a bimetallic alloy, a sufficiently strong reducing agent must be used. Previous work done by the DiSalvo group at Cornell showed that reduction of these salts with either $NaBH_4$ or sodium naphthalenide would result in alloy formation, however no attempts were made by them to deposit this alloy onto a carbon support.

The second method, and the more novel approach, is accomplished by the thermal reduction of a single-source precursor containing both lead and platinum. Since the overall stoichiometry of the precursor is 1:1, there exists only one stable alloy of which to form. Previous work in the Lukehart lab has focused on the preparation of a number of nanoparticles of bimetallic alloys from these types of precursors.[50]

The use of carbon supports solves multiple issues in electrocatalysis. Firstly, particle nucleation can occur on the surface of the carbon support, preventing the formation of large particles. Secondly, the carbon support increases the conductivity of these composite samples, allowing for greater performance in devices. Specifically, graphitic carbon nanofibers have shown to produce a large increase in the performance of Pt_1Ru_1 alloy materials.

GCNFs are grown from the reduction of carbon monoxide over an iron nickel catalyst supported on fused silica. After growth, the catalyst material is removed by

washing with hydrofluoric acid and the fibers are cut using an ultrasonicator. This results in nanofibers with a length of roughly 100 nm and a width of 10-25 nm.

Initial attempts to replicate the work of the DiSalvo group were unsuccessful.[51,52] The co-reduction of a methanolic solution of hexachloroplatinic acid and lead acetate in the presence of a GCNF support material resulted in the production of Pt/GCNF nanocomposites and contained a large amount of partially oxidized lead species, but no ordered alloy product formation was observed.

Since the platinum salt was preferentially reduced, other platinum precursors were studied to determine if a slight increase in the reduction potential could drive the formation of alloy nanoparticles. Switching the platinum precursor to K_2PtI_6, which should have increased electron density on the platinum metal center due to pi back bonding of the iodide ligands, results in the successful formation of ordered PtPb/GCNF nanocomposite materials.

XRD analysis of these nanocomposite shows that the PbPt alloy is the only crystalline product formed **(Figure 12).** Scherrer's analysis of this PtPb/GCNF alloy shows an average particle size of around 5.94 nm, which is in agreement with a histogram plot from the TEM data on this sample which shows the average size to be 5.39 nm. The agreement of these two measurements indicates that there are no large particles present in the sample. The metal loading of this sample is determined by temperature programmed oxidation under a carbon dioxide atmosphere. When these nanocomposites are heated under CO_2, the metal atoms are undisturbed, but the carbon support is oxidized. TPO studies show the metal loading of this sample to be around 60 weight % **(Figure 13).**

Additionally, the stoichiometry of the metals present can be determined by ICP-OES. The nanocomposite is burned in air to remove the carbon support, then digested in hot nitric acid to dissolve the lead, followed by treatment with hot aqua regia to dissolve the platinum. ICP-OES results indicate that the sample contained 50.7 % Pt and 49.3% Pb, close to that of the desired 1:1 alloy. The TEM data also shows good particle dispersity across the carbon surface **(Figure 14).**

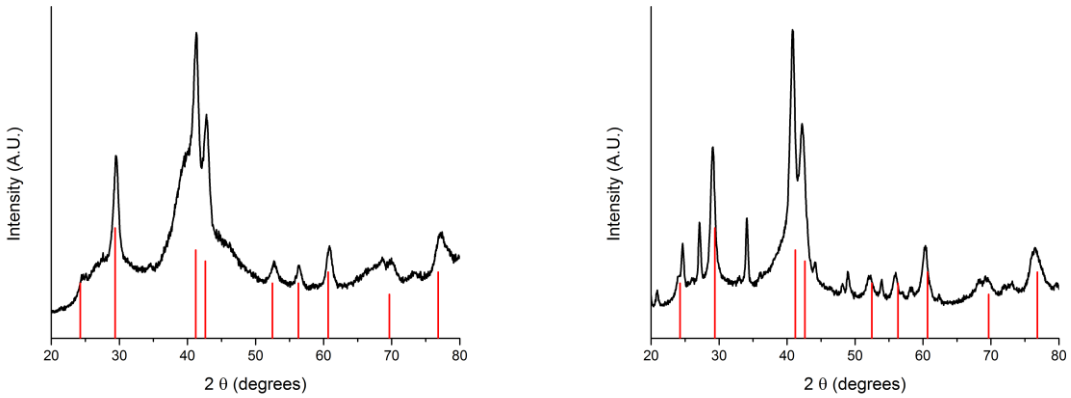

Figure 12. XRD patterns of PtPb/C samples synthesized by solution metal ion reduction. (left) JCB-2-15-4, (right) KCP-1-23. Red drop lines indicate bulk PtPb (PDF#06-0734)

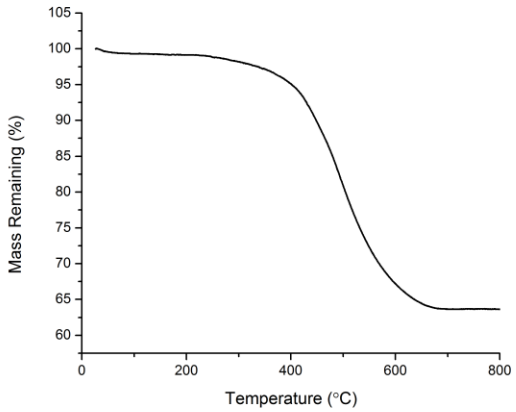

Figure 13. Temperature programmed oxidation of JCB-2-15-4 under carbon dioxide atmosphere

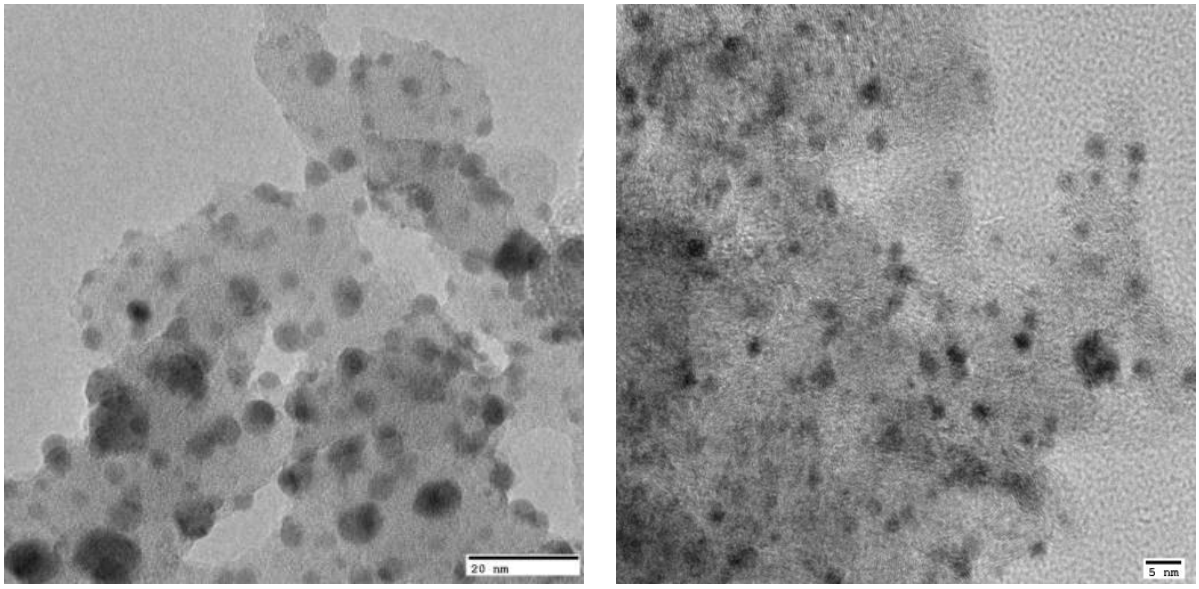

Figure 14, TEM images of solution metal ion reduction PtPb/C samples. (left) JCB-2-15-4, (right) KCP-1-23

Single-source precursor design is a challenging step in the development of an alloy by thermal reduction. Not only does the molecule need to contain both metal species, but the extraneous ligands must also not decompose to form stable phases with these metals. While there are many molecules that contain a lead-platinum bond, a large majority of these molecules contain phosphine ligands, which will thermally decompose to form Pt-P

phases. To remove the possibility of this impurity forming, substitutions from phosphine ligands to nitrogen based ligands, such as bipyridine and anthracene derivatives, were chosen, as there are no known stable Pt-N or Pb-N phases.

The synthesis of the single-source precursor begins with the reaction of $PtCl_2(SEt_2)_2$ with excess CH_3Li. The methyl group exchanges with the chloride to form the dimeric species $[Pt(CH_3)_2(SEt_2)]_2$. The isolated $[Pt(CH_3)_2(SEt_2)]_2$ then reacts with two equivalents of Ph_2Me_2Phen which displaces the SEt_2 ligands to yield $Pt(CH_3)_2(Ph_2Me_2Phen)$, a reddish-orange molecule. This molecule is then dissolved in THF and solid $PbPh_2Cl_2$ is added, which results in oxidative addition across a Pb-Cl bond to form the single-source precursor $Pt(CH_3)_2(Ph_2Me_2Phen)(PbPh_2Cl)Cl$. Interestingly, the oxidative addition reaction only occurs in ample sunlight, suggesting it may be a radical-driven mechanism. Another single-source precursor, in which the Ph_2Me_2Phen was replaced with bipy was also synthesized, but is not stable in any solvent it is soluble in, therefore it was not used to create a PbPt/C catalyst sample.

To obtain a nanocomposite from the thermal reduction of a single-source (SS) molecular precursor, a carbon support is impregnated with the precursor molecule, dried, and resuspended in a solvent the precursor is not soluble in. This suspension is then deposited on a silicon wafer to ensure that no sintering of the particles occurs during decomposition **(Figure 15).**

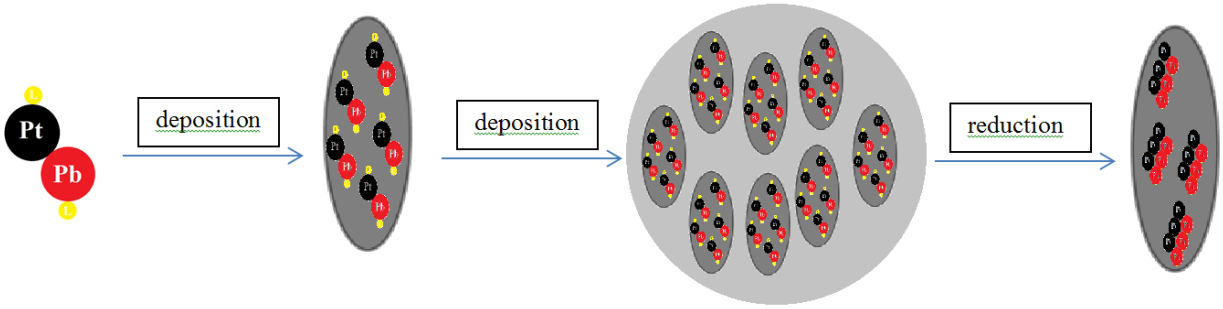

Figure 15. Cartoon depiction of the synthesis of PtPb/C composites by reduction of a single-source molecular precursor

XRD analysis of this PtPb/C nanocomposite indicates the formation of PtPb as the major crystalline product **(Figure 16).** Although the peak broadening is not as pronounced as in the solution metal ion reduction sample, Scherrer's analysis can only typically be done on particle size less than 10 nm. TEM images confirm the presence of particles with an average size of 20 nm, supported on a carbon surface. Additionally, on particle EDS analysis confirms the stoichiometry of these particles to be close to 1:1, indicating that the reduction of the single-source molecular precursor is successful and contains no other elements **(Figure 17).**

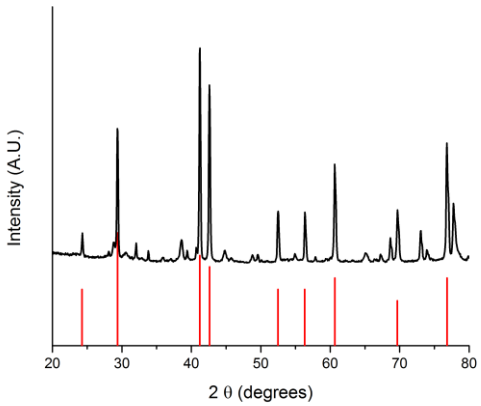

Figure 16. XRD pattern of PtPb/C synthesized from a single-source molecular precursor. Red drop lines indicate bulk PtPb (PDF#06-0734)

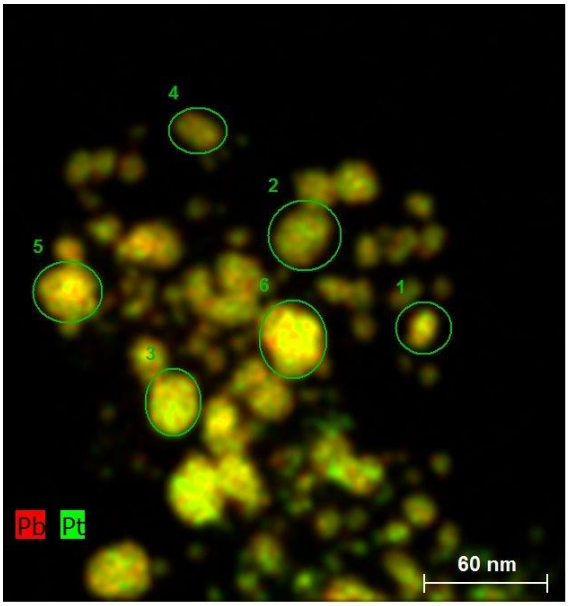

	Particle 1	Particle 2	Particle 3	Particle 4	Particle 5	Particle 6	Overall
Platinum atomic %	47.45	48.99	50.77	46.93	47.19	48.24	46.02
Lead atomic %	52.55	51.01	49.23	53.07	52.81	51.76	53.98

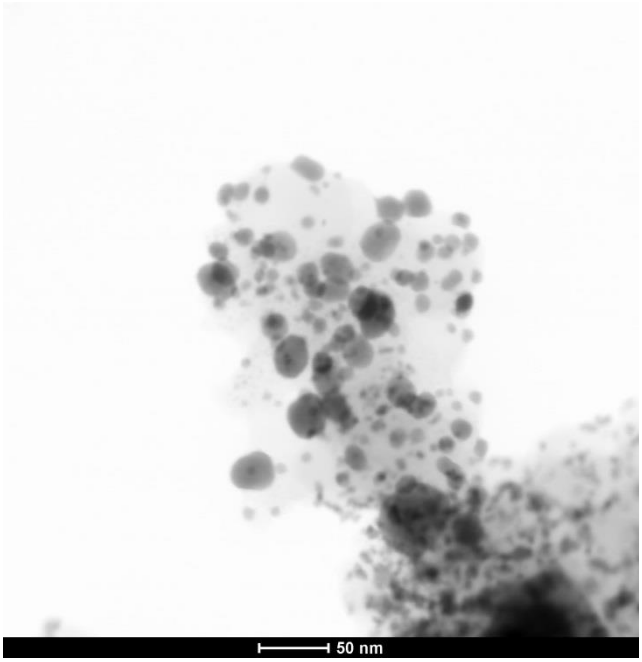

Figure 17. TEM images of SS-PtPb/C. On particle EDS confirms stoichiometry of material

Electrochemical Analysis of PbPt/C nanocomposites

Electrochemical analysis of catalysts synthesized from solution metal ion reduction showed interesting results. Sample JCB-2-15-4, of which XRD, TEM and ICP-OES analysis showed had great speciation towards a PtPb alloy, did not perform well. The cyclic voltammetry experiments showed almost no hydrogen adsorption, indicating that the surface does not contain a large amount of platinum atoms. Conversely, sample KCP-1-23 which is lead rich and contains an unknown species by XRD, performed quite well **(Figure 18)**. Hydrogen adsorption is evident on the surface of this catalyst. Additionally, rotating disk experiments in formic acid showed that KCP-1-23 had a lower onset for formic acid oxidation, almost 0.05 V lower than JCB-2-15-4. It is possible that the presence of more lead on the surface of JCB-2-15-4 blocks catalytically active platinum sites from oxidizing the fuel. Another possibility is that the unknown XRD phase is catalytically active for formic acid oxidation and is the active species in KCP-1-23. Although KCP-1-23 was active for formic acid oxidation, the activity is quite low in comparison to other PtPb samples, so other synthetic routes were explored.

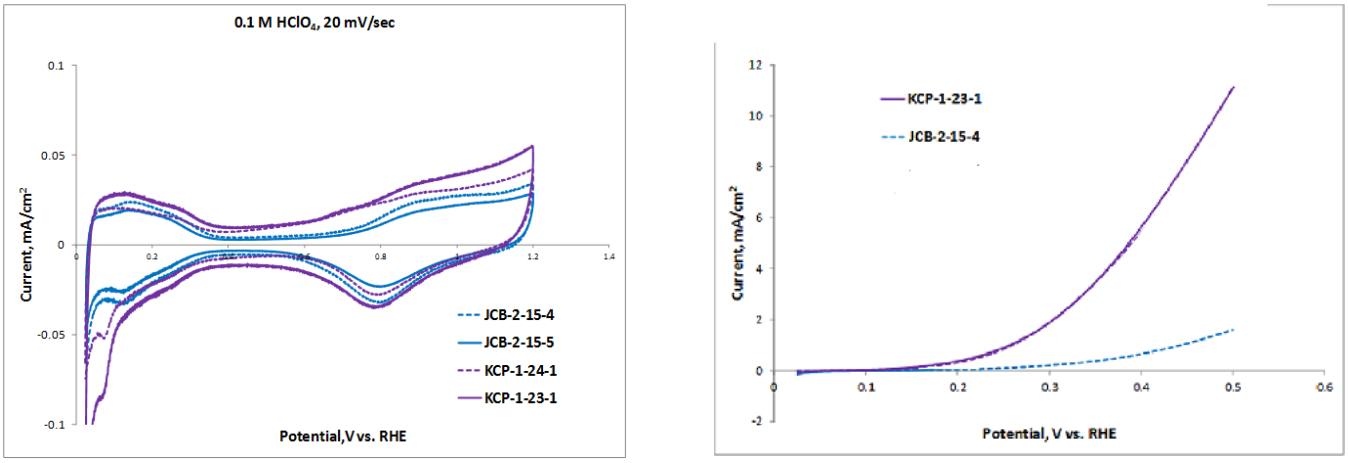

Figure 18. Electrochemical analysis of SMIR PtPb/C. (left) CV scans in 0.1 M $HClO_4$. (right) RDE scans at 0.3 V (vs. RHE)

A sample was synthesized from a single-source precursor and analyzed for its ability to oxidize formic acid. The CV scan, taken in sulfuric acid, is very promising **(Figure 19**). Hydrogen adsorption is evident, indicating the presence of platinum on the surface of the catalyst, while the oxidation of platinum at 0.3 V (vs. Ag/AgCl) is also seen. When performing the same experiment in 0.5 M formic acid, the onset potential of oxidation is -0.1 V (vs. Ag/AgCl). Additionally, a second oxidation peak is seen on the reverse scan. This indicates that while some platinum is incompletely oxidizing formic acid, the adjacent lead atoms are participating in the successive oxidation of carbon monoxide to carbon dioxide, re-opening the platinum sites for catalysis. With this promising result, rotating disk electrode studies were pursued to determine the stability of this catalyst.

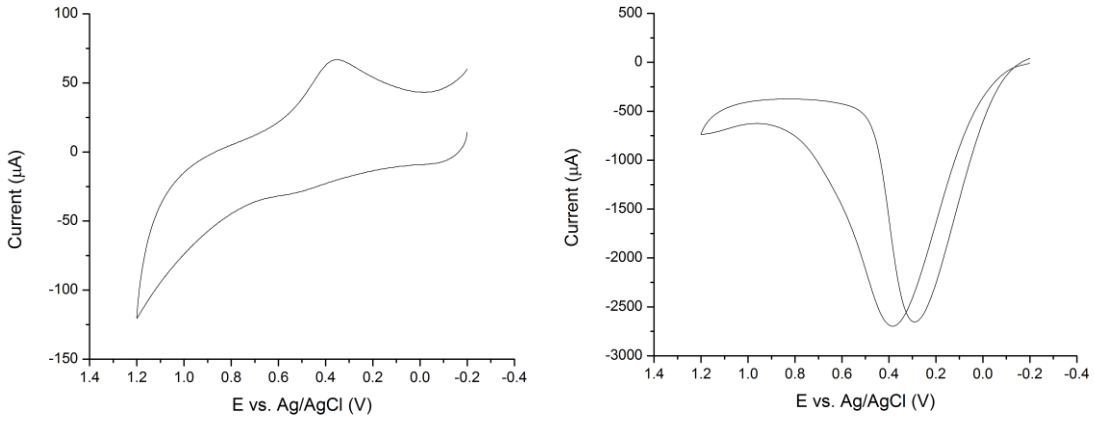

Figure 19. Electrochemical analysis of SS-PtPb/C. (left) CV in 0.1 M H_2SO_4. (right) CV in 0.5 M formic acid

Amperometric curves were taken under the same conditions as the CV scans, with the voltage held at 0.2 V (vs. Ag/AgCl); at this overpotential, the rate of formic acid oxidation is exponentially higher than at the onset potential at the cost of some efficiency of the device. Initial current values were around -140 mA/mg metal, which is quite good relative to other

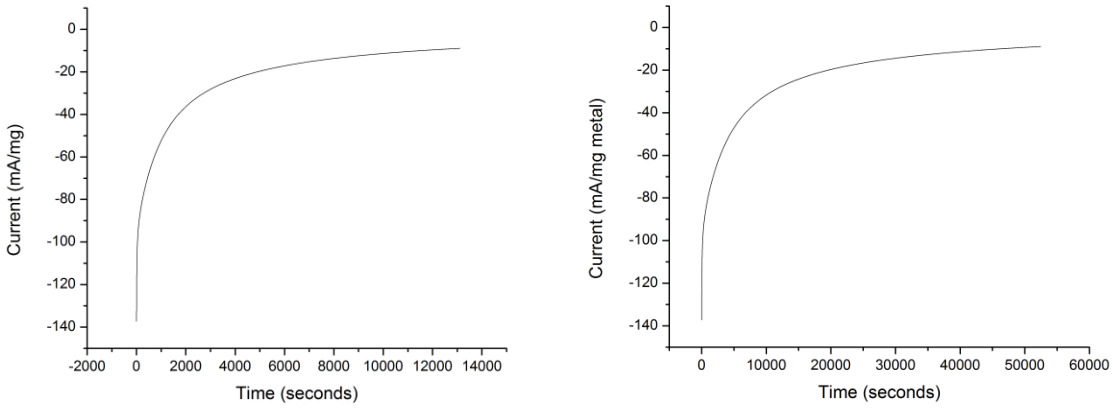

Figure 20. Successive RDE studies on SS-PtPb/C. After new fuel was added, initial current returned to original value showing no degradation of catalyst material

PtPb catalysts **(Figure 20).** However, the current dropped 50% within the first 10 minutes, and proceeded to drop over the course of several hours. After 3.5 hours, the current had dropped to around 10 mA/mg metal. When the fuel was replaced, and the study continued, current values were again around -140 mA/mg metal. This indicates one of two possible outcomes. Firstly, the catalyst is consuming fuel rapidly, and the drop in current is due to the lack of fuel present in the system. Secondly, the carbon dioxide formed at the surface of the catalyst is not able to leave and becomes trapped on the surface, which would lead to a decrease in catalysis.

Conclusion

A range of compositions of PdAu/C catalysts was prepared by solution-metal ion reduction for their ability to generate hydrogen in combination with a direct methanol fuel cell. While some catalysts showed good activity for the production of hydrogen, no correlation to catalytic activity and composition could be discerned. In future samples, XPS of the surface could elucidate more information about the arrangement of metal atoms on the surface of these catalysts.

Additionally, alloys of tantalum, oxygen and nitrogen were studied for their ability to catalyze the oxygen reduction reaction. While several samples were synthesized in between the range of Ta_2O_5 and Ta_3N_5, no samples showed ORR activity. The incorporation of carbon could be required for the ORR activity seen in other transition metal materials . With the current synthetic method, the use of a graphite tube furnace capable of reaching temperatures in excess of 1500 °C might be required for carbon incorporation.

Lastly, PtPb/C catalysts for formic acid oxidation were synthesized by solution-metal ion reduction and the thermal reduction of a single-source molecular precursor. Solution-metal ion reduction samples had an impurity as seen by XRD data, the composition of which has not been discerned. These samples, in general, had low activity for formic acid oxidation. The samples synthesized by thermal reduction of a single-source precursor, however, show good speciation as seen in XRD data, and are catalytically active for formic acid oxidation. The longevity of these catalysts, as well as their durability to higher concentrations of formic acid, are still being investigated.

Chapter III: Quantitative X-ray Diffraction of Clay Minerals of the Brahmaputra River Delta

Introduction

X-ray Diffraction

X-ray diffraction is a powerful analytical tool for the rapid identification of organic and inorganic materials and compounds. X-ray diffraction works by applying a large accelerating voltage across a sharp tungsten filament. This ejects electrons from the filament which travel towards the target of the x-ray tube, generally copper or molybdenum metal. When the electron hits this target material, 99% of the collisions result in thermal relaxation. The other 1 % of collisions results in the ejection of an electron from the shell of the target material. As a higher energy electron fills in this hole, an x-ray is generated. These electrons are then collimated through small slits and diffract off the electron density of atoms in the sample material according to Bragg's law:

$$n\lambda = 2d \sin\theta$$

Where n is an integer, λ is the wavelength of the x-ray, d is the interatomic spacing of the atoms in the material, and θ is the angle between the sample and sample. When Bragg's law is met, the diffracted x-ray is constructively interfered with and a signal is seen at the detector. When Bragg's law is not met, diffracted x-rays are destructively interfered with and no signal is recorded.

Identification of materials is the most widely used application of x-ray diffraction. As the interatomic spacing of atoms is dependent on the atoms identity, as well as the space group of the material, most XRD patterns are unique to a given material. Quantification of materials is also possible using XRD, but is not as widely used.

Quantification is most easily accomplished with the use of an internal standard. A specific amount of an internal standard is added to the sample of interest and the peak areas are compared against a calibration curve of a known quantity of both materials. The best choice for an internal standard is a highly crystalline material with a well-defined particle size and no peak overlap with the material of interest.

Weathering of Clay Minerals

Clay minerals are an essential part of the Earth's crust and contain information about the history and environment of the geologic areas they are found in. The identification of different clay minerals in soil is essential to agriculture for the determination the amount of moisture the soil will hold, and whether there are any natural fertilizers in the field. Clay mineralogy is also important in many engineering fields as the types of clay present in an area can determine whether or not that piece of land is suitable for the construction of buildings.

Additionally, the weathering of clays can give us information about the history of the area they were found in. As clays are exposed to moisture and oxygen from the ambient environment, they can weather and erode into other clay minerals. The presence or lack of these minerals gives information on when the areas at the depth of the clays were last present on the surface **(Figure 1**). This is important in reconstructing the geologic landscape of a region after a major event such as an earthquake or flood occurs.

Experimental Methods

Collection of Sediment Samples

Boreholes were drilled along the apex of the fluvial fan of the Bengal River Delta and assigned a five digit sample ID, BNGAXXXØØ, where XXX indicates the distance from the

fluvial fan in kilometers and ØØ indicates the depth of the borehole samples in meters. These sediment samples were then sub-divided into smaller sets based on surface-weighted particle diameters, of which the fraction with diameters < 62.5 μm were selected for x-ray diffraction measurements.

Preparation of mud samples

Selected sediment samples were wet sieved from a solution of sodium hexametaphosphate through a 2.5 μm sieve. Particles below this size are considered to be clay minerals.

X-ray Diffraction

X-ray diffraction patterns were collected on a Scintag X-1 Powder X-ray Diffractometer equipped with a copper target and a Peltier cooled solid-state detector. The powders were analyzed for the semi-quantification of four minerals [illite, smectite, chlorite and kaolinite], as well as the presence of goethite. Three analyses were conducted; the powders were first scanned without any modification, then they were placed onto watch glasses into a bell jar with an open beaker of ethylene glycol at 60 °C for 3 days to saturate the powders with ethylene glycol (glycolated samples) to resolve smectite and illite, and lastly the powders were heated in a tube furnace at 500 °C in open atmosphere to remove the presence of kaolinite and quantitate chlorite. The presence of goethite was analyzed by overlaying PDF#29-713 [goethite FeO(OH)].

Semi-quantification of clay minerals

Semi-quantification was determined using a previously described method, which is based on relative peak areas of the four minerals. Peak areas were determined using

CasaXPS software. A ratio of quartz:clay was also determined using a zinc oxide internal standard that was referenced against a calibration curve of zinc oxide and quartz powders.

Results and Discussion

Clay minerals were analyzed for smectite (5.2 °2 θ), illite (8.8 °2 θ), chlorite (12.3 °2 θ),, and kaolinite (12.3 °2 θ), which are identified by the *d*-spacing of their most intense reflection. As smectite and illite share a reflection, quantification of these minerals requires some way to separate them. Smectite is known as a swelling clay, which means that when exposed to solvent, the solvent molecules are able to intercalate the layers of this clay material, thereby increasing the *d*-spacing of these layers. Illite does not swell in the presence of these solvents.

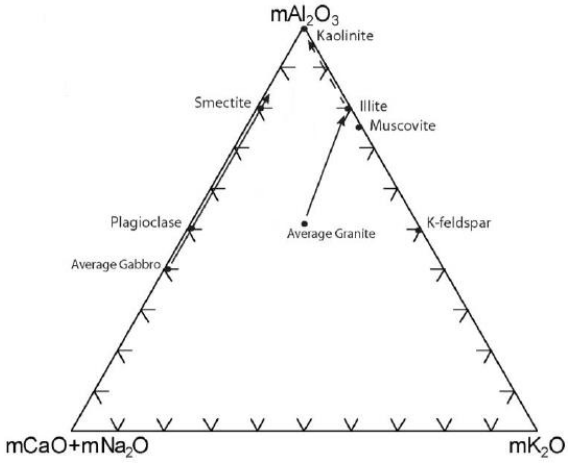

Figure 1. Weathering diagram of clay minerals

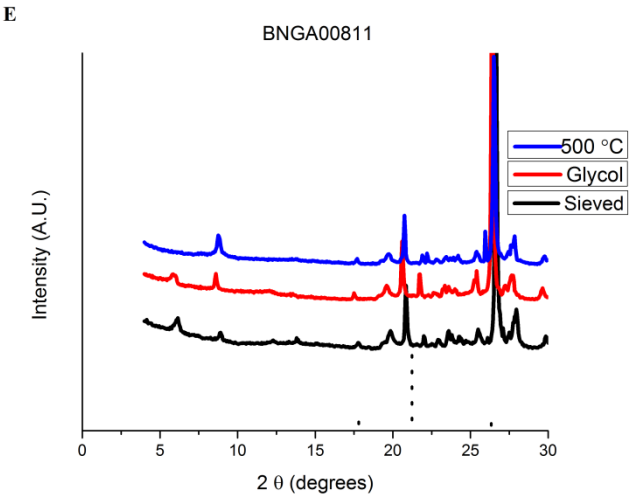

Figure 2. XRD pattern of BNGA00811, indicating the presence of illite, smectite and chlorite

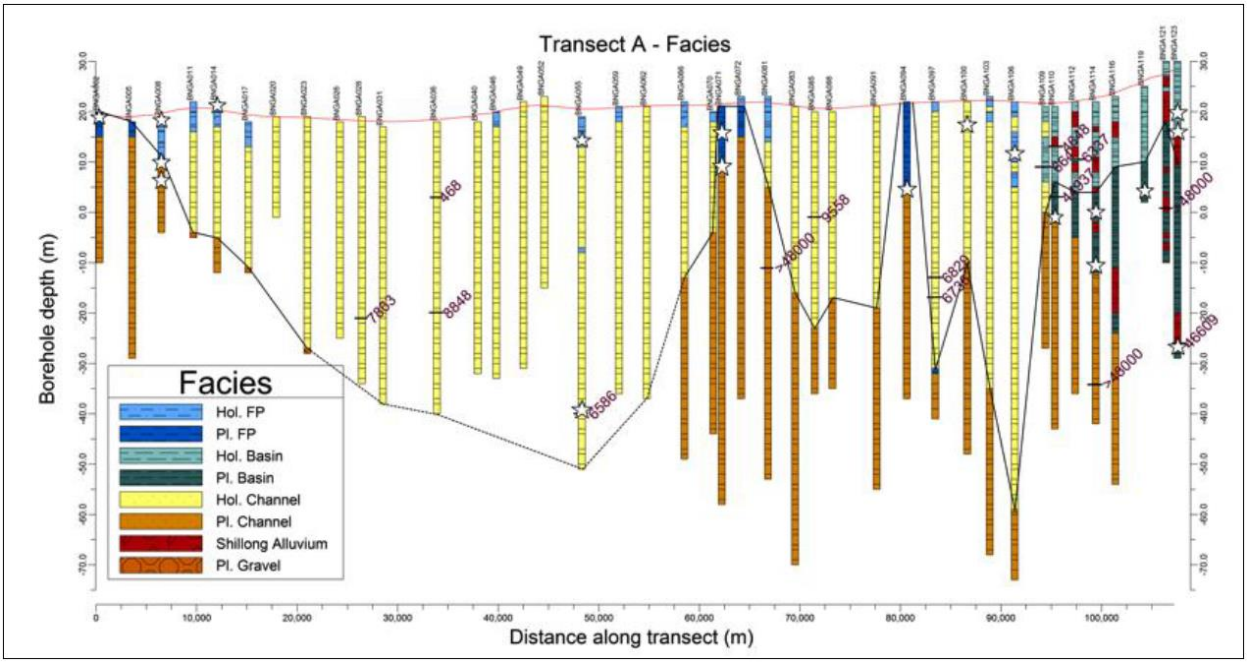

Figure 3. Map of borehole locations of sediment samples along transect A.

Additionally, kaolinite and chlorite also share a reflection, and they must also be separated. Kaolinite is unstable in air above 350 °C, so heating a sample above this temperature would result in no kaolinite being present, so all diffraction intensity at 12.3 ° 2 θ is due to chlorite. Qualitative analysis of these clay minerals is seen in an example XRD pattern **(Figure 2).** In additional the qualitative analysis, these clay minerals can also be

semi-quantitatively analyzed in reference to themselves. Since these sediments were sieved below 2 μm, clay minerals are the only species present. Comparison of peak areas results in the semi-quantitative analysis found in Appendix A, along with all representative XRD patterns.

Quantification of clay:quartz ratios is easily determined with the use of an internal standard. Zinc oxide is an abundant material well-suited to be used in quantitative analysis. First, a calibration curve was constructed with known ratios of zinc oxide to quartz powder compared against the ratio of their peak areas. This calibration curve is then used to determine the mass of quartz present in a sample after the addition of zinc oxide to that sample. Quartz:clay ratios are seen in Appendix A.

From these accumulated data, three areas of distinct clay minerology can be determined **(Figure 3).** Zone I encompasses the Bogra Terrace, Jamulpur Terrace and Sherpur Remnant, and is characterized by the presence of almost entirely illite in the clay sediments. Feldspar minerals in this zone are transforming into silicate materials like illite. This area in not currently accumulating sediment, and the sediment present is not being weathered. It can be characterized as a dry, elevated zone. Zone II encompasses the Dauki Foredeep. In this zone, sediment is slowly accumulating at the rate of 1 cm/year and is being uplifting by the underlying Dauki fault. Lastly, zone III, which encompasses the Brahmaputra braidbelt, is in active accretion, with a large influx of sediment and subsequent weathering due to the flow of water through the delta region.

Conclusion

In conclusion, quantitative XRD analysis of several clay samples from the Bengal River Delta has been accomplished through the use of an internal standard, zinc oxide.

Additionally, qualitative analysis of goethite, illite, smectite, chlorite, and kaolinite has been accomplished through the use of glycolation and calcination to achieve separation between two minerals which have overlapping XRD reflections.

Appendix A. X-ray Diffraction Patterns of Clay Minerals from the Upper Bengal Basin.

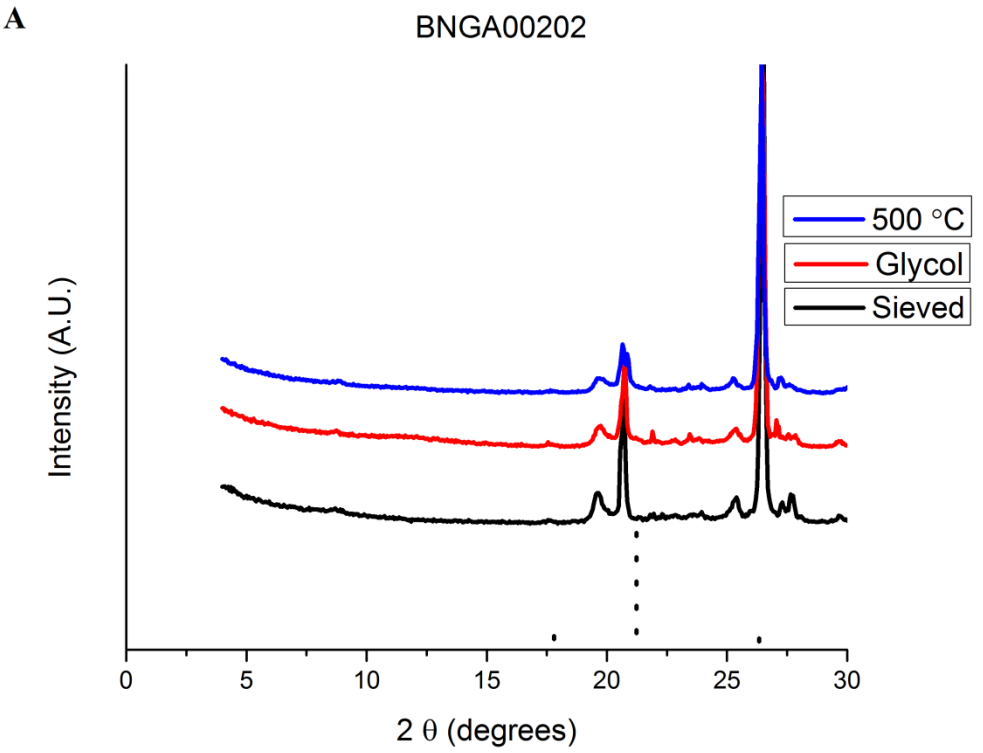

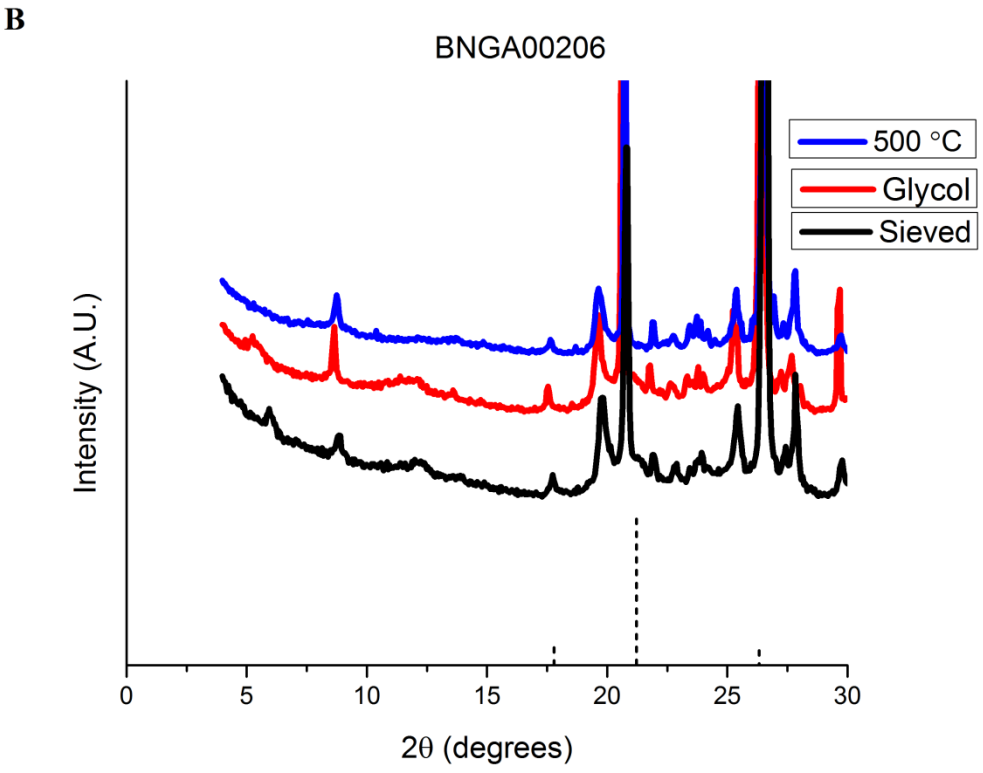

C

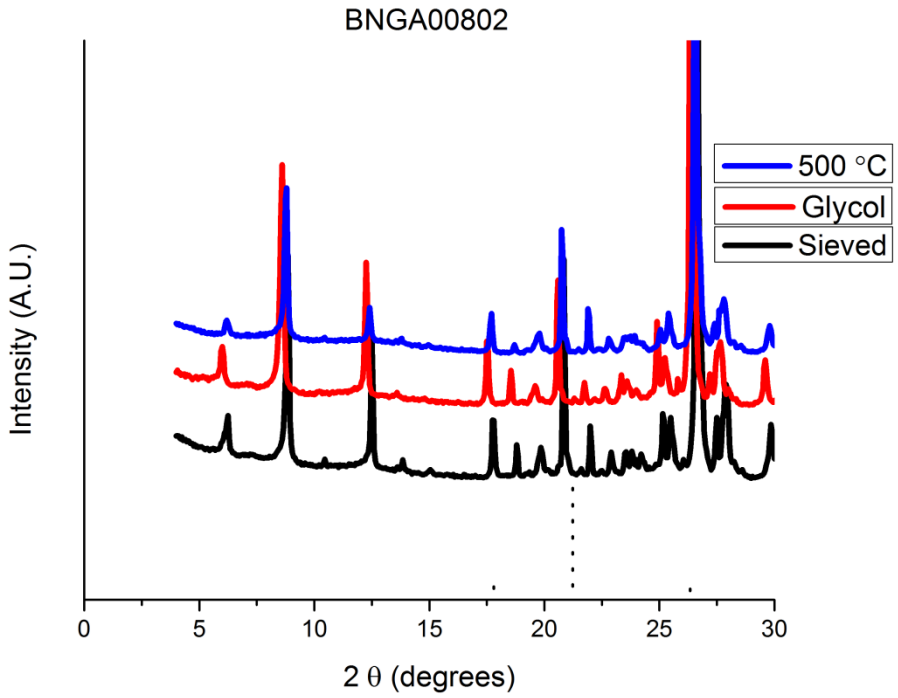
BNGA00802
Intensity (A.U.)
2 θ (degrees)
0
5
10
15
20
25
30
500 °C
Glycol
Sieved

D

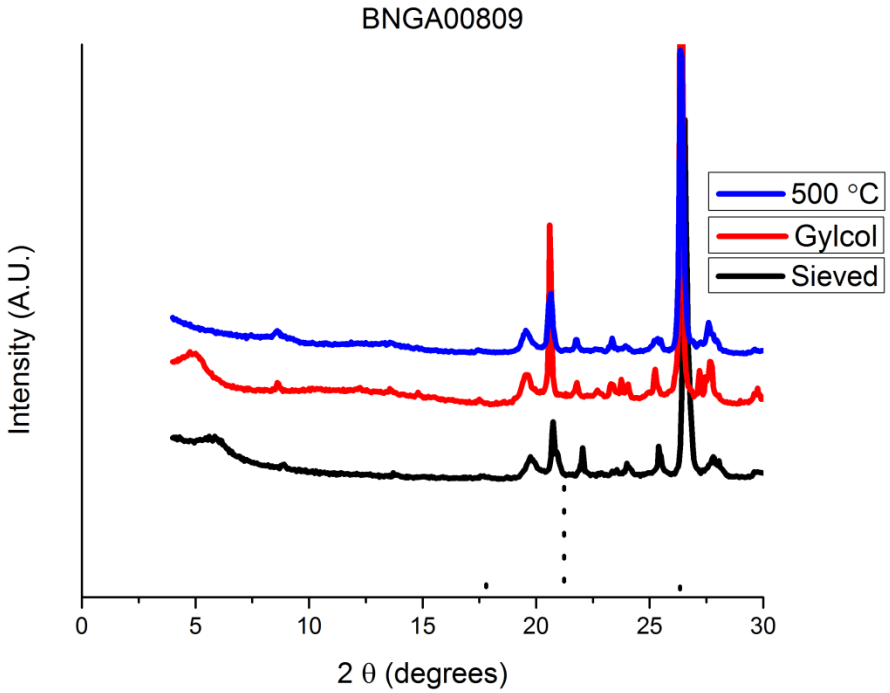
BNGA00809
Intensity (A.U.)
2 θ (degrees)
0
5
10
15
20
25
30
500 °C
Gylcol
Sieved

E

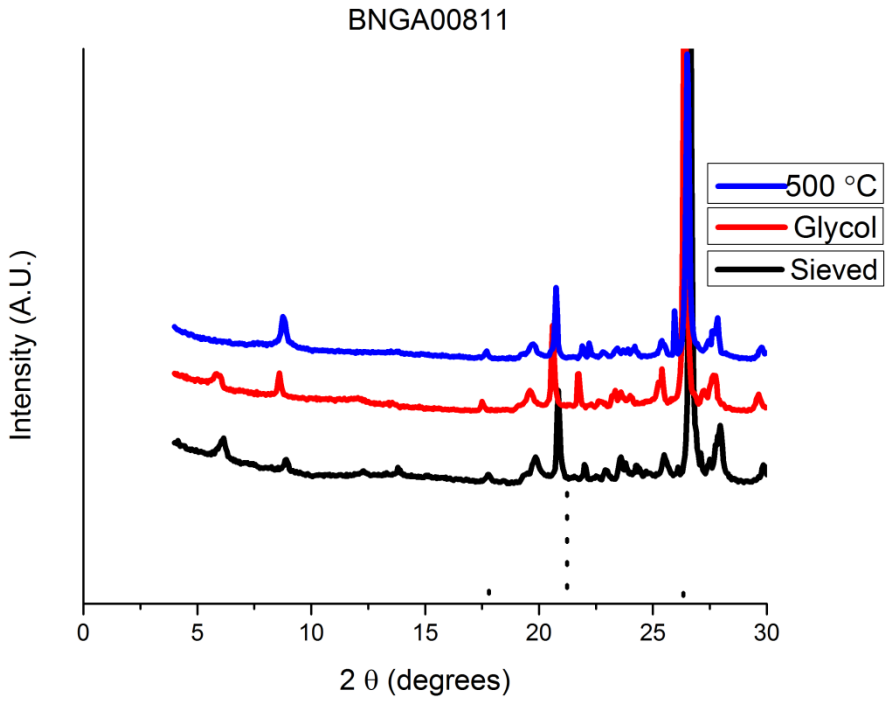
BNGA00811
500 °C
Glycol
Sieved
Intensity (A.U.)
0
5
10
15
20
25
30
2 θ (degrees)

F

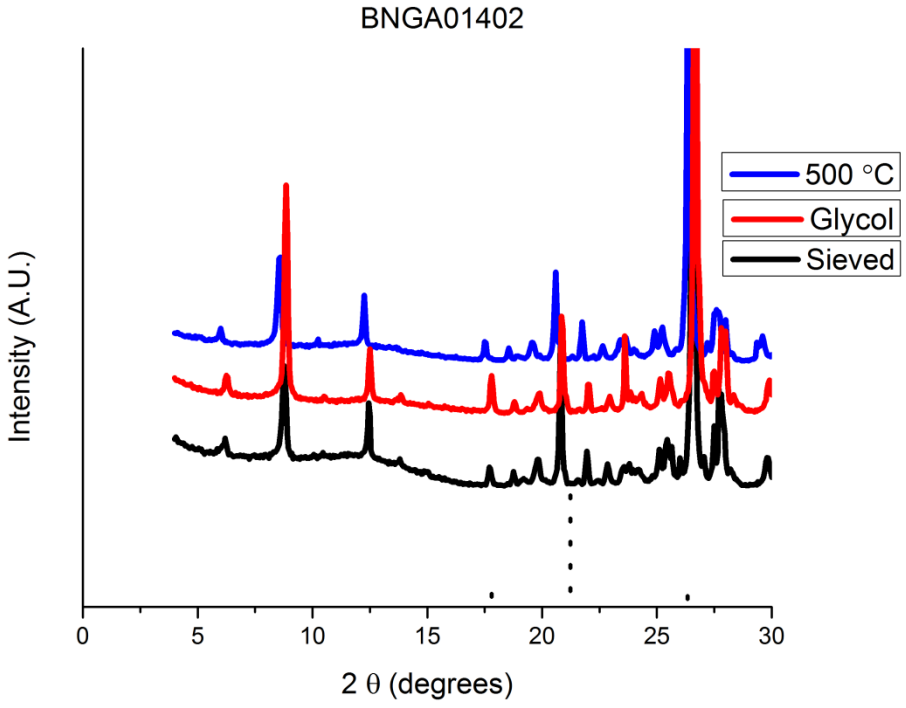
BNGA01402
500 °C
Glycol
Sieved
Intensity (A.U.)
0
5
10
15
20
25
30
2 θ (degrees)

G

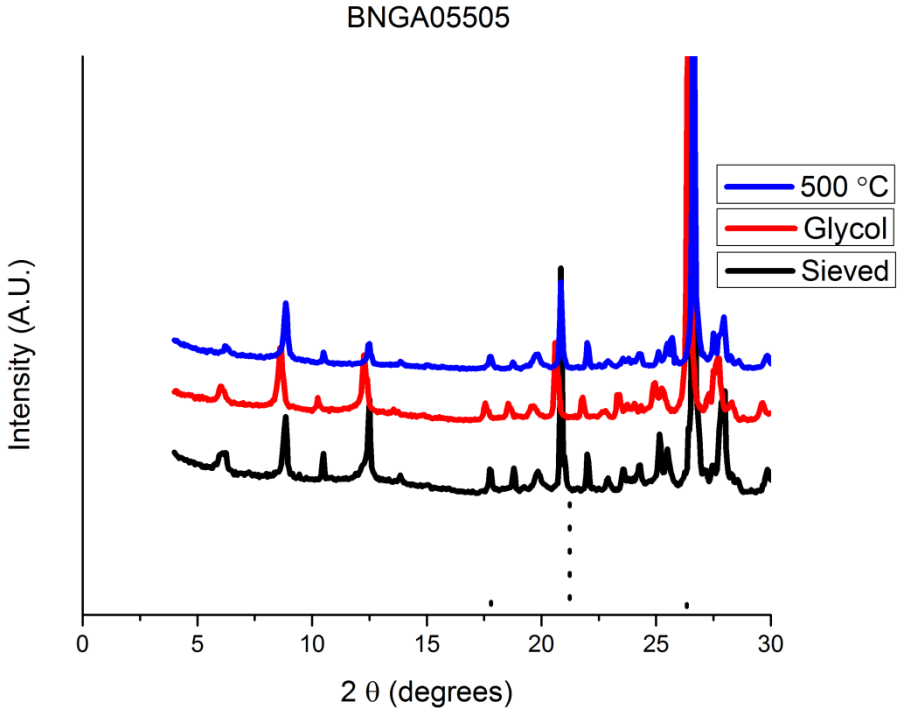
BNGA05505
500 °C
Glycol
Sieved
Intensity (A.U.)
0
5
10
15
20
25
30
2 θ (degrees)

H

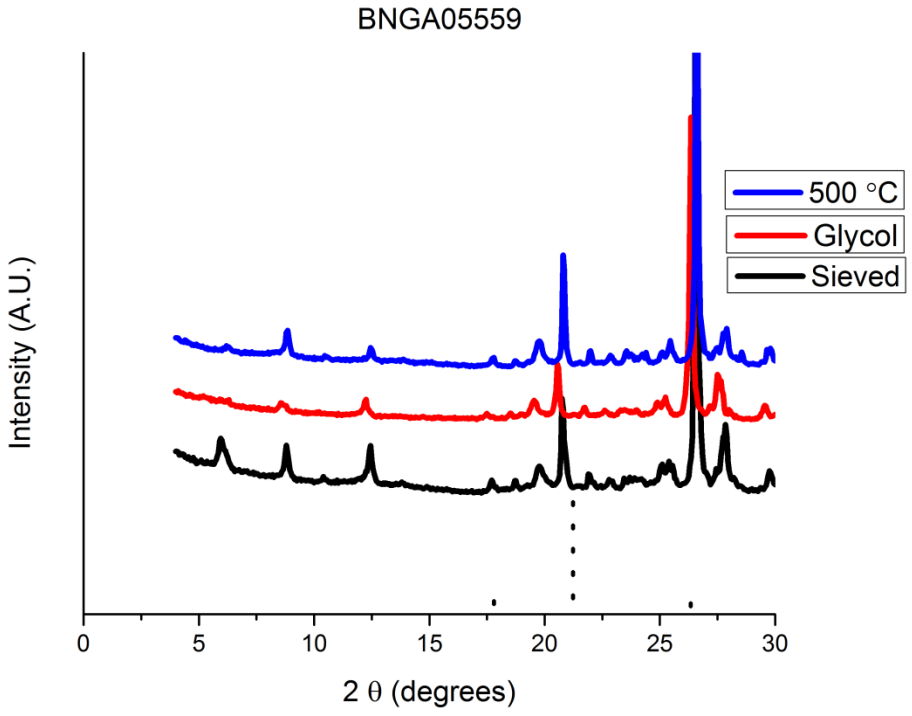
BNGA05559
500 °C
Glycol
Sieved
Intensity (A.U.)
0
5
10
15
20
25
30
2 θ (degrees)

I

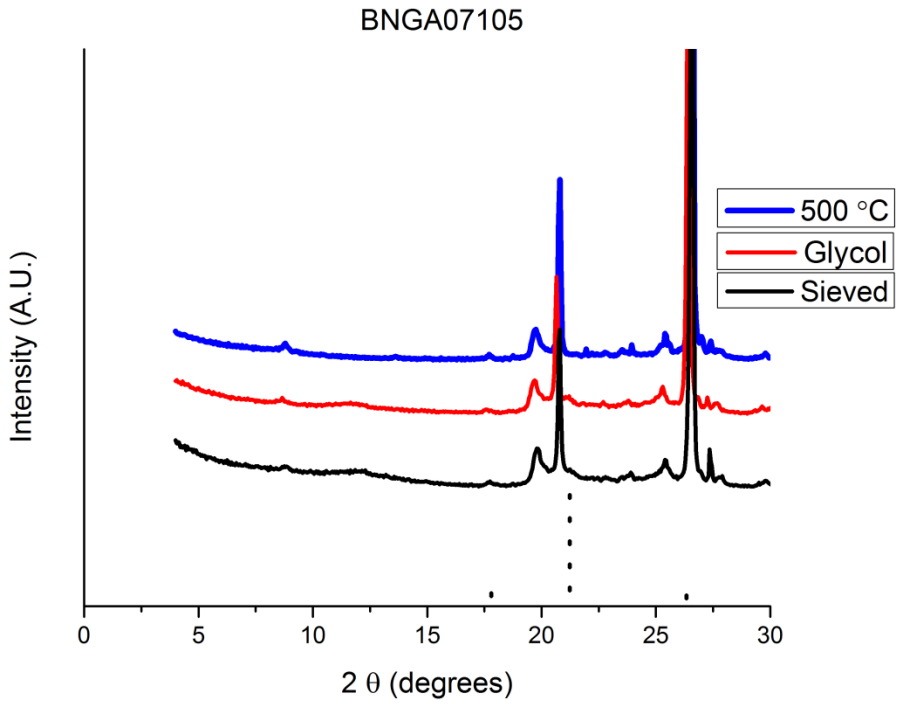
BNGA07105
Intensity (A.U.)
2 θ (degrees)
0
5
10
15
20
25
30
500 °C
Glycol
Sieved

J

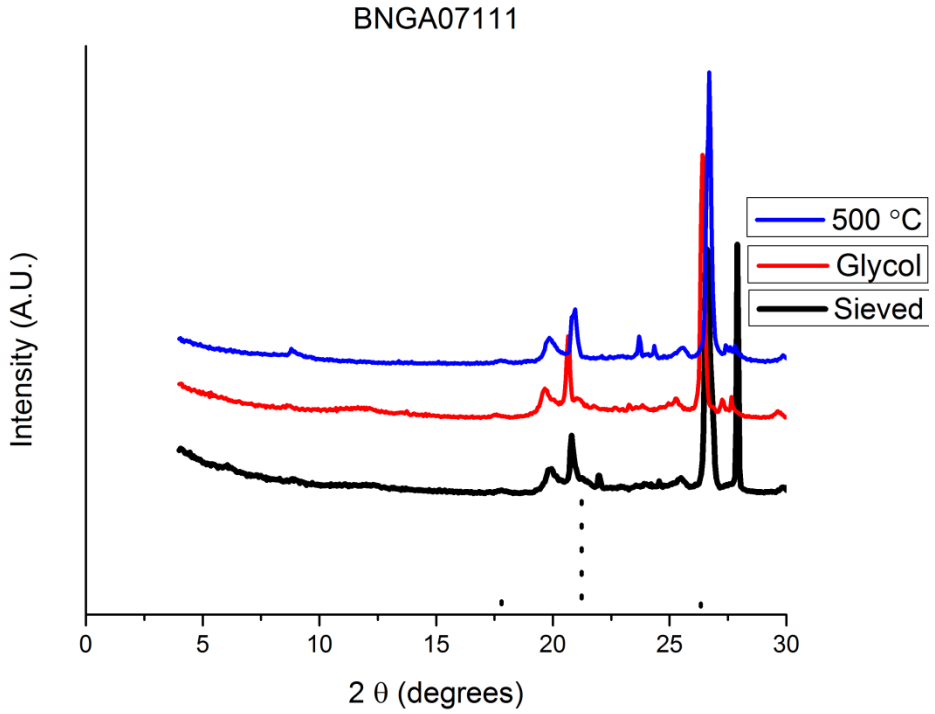
BNGA07111
Intensity (A.U.)
2 θ (degrees)
0
5
10
15
20
25
30
500 °C
Glycol
Sieved

K

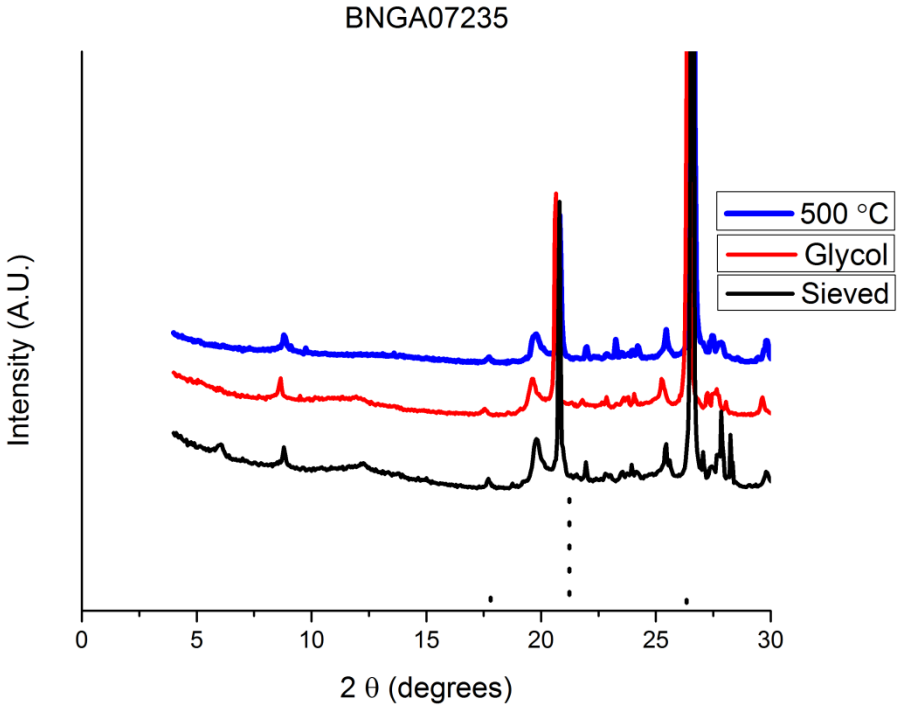
BNGA07235
Intensity (A.U.)
2 θ (degrees)
0
5
10
15
20
25
30
500 °C
Glycol
Sieved

L

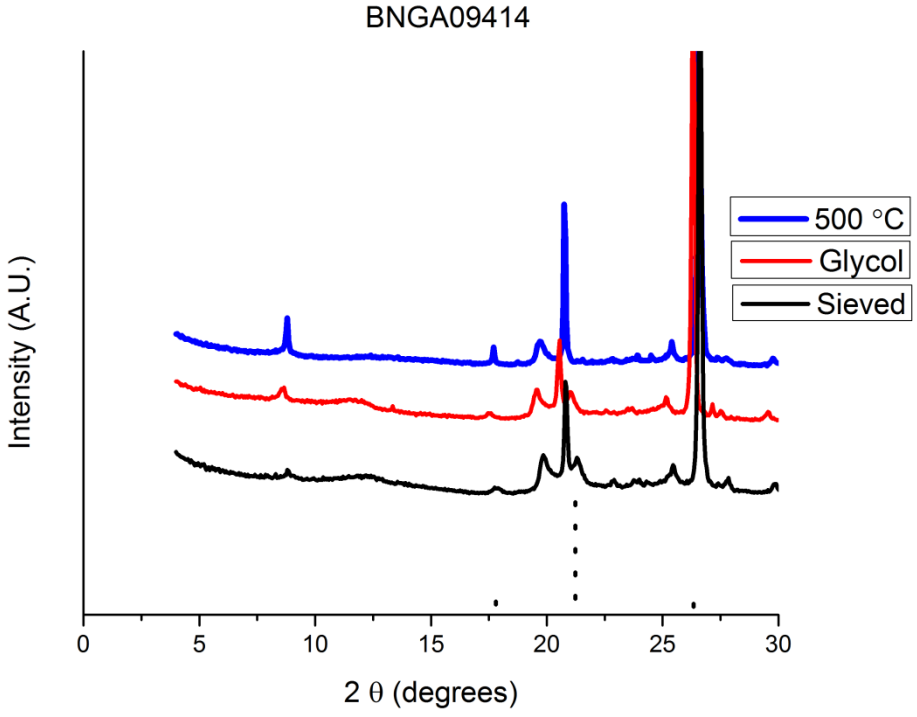
BNGA09414
Intensity (A.U.)
2 θ (degrees)
0
5
10
15
20
25
30
500 °C
Glycol
Sieved

M

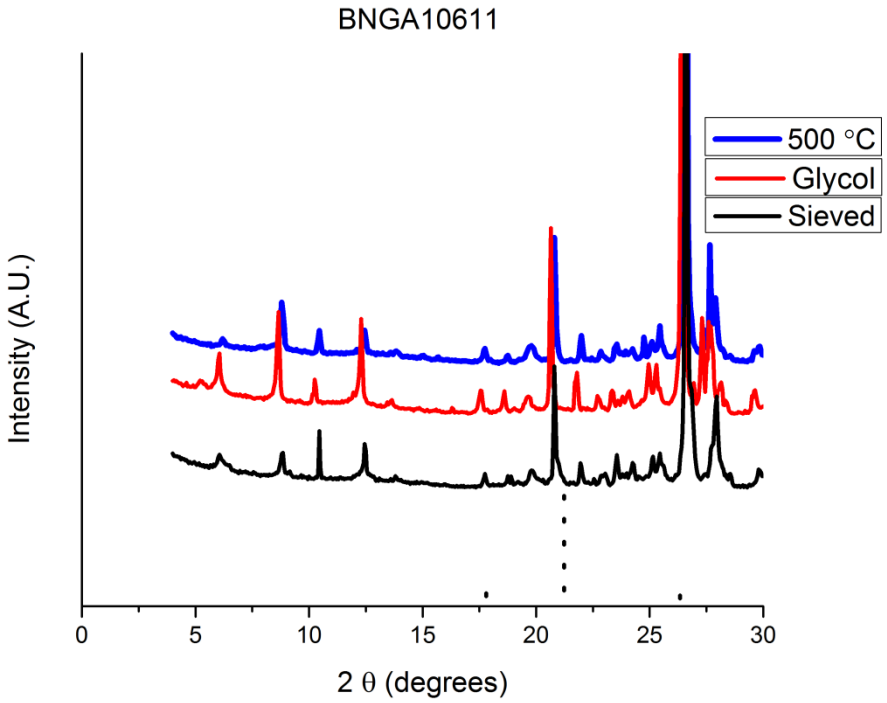
BNGA10611
500 °C
Glycol
Sieved
Intensity (A.U.)
0
5
10
15
20
25
30
2 θ (degrees)

N

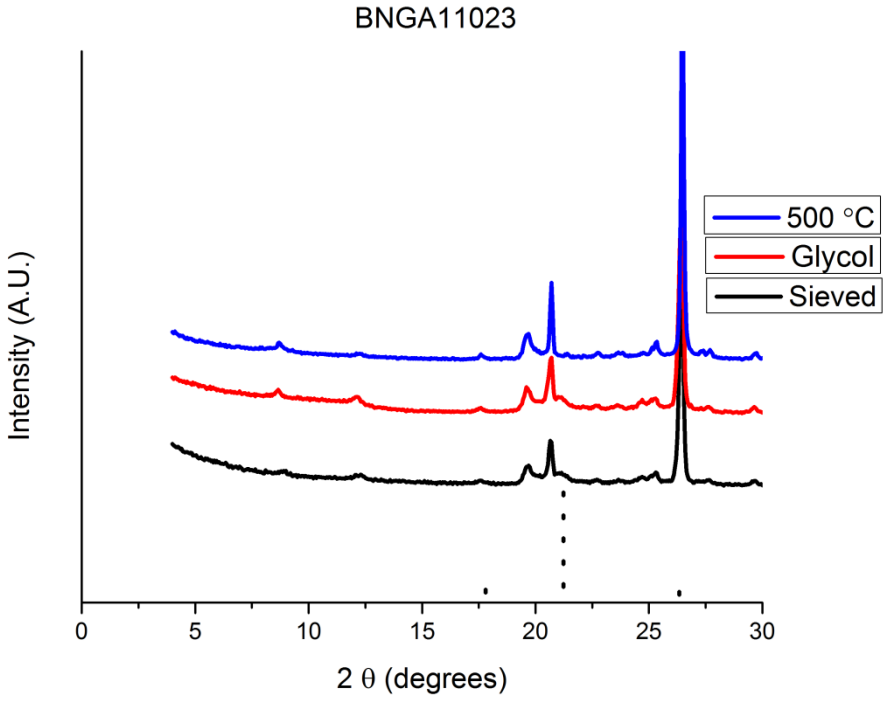
BNGA11023
500 °C
Glycol
Sieved
Intensity (A.U.)
0
5
10
15
20
25
30
2 θ (degrees)

O

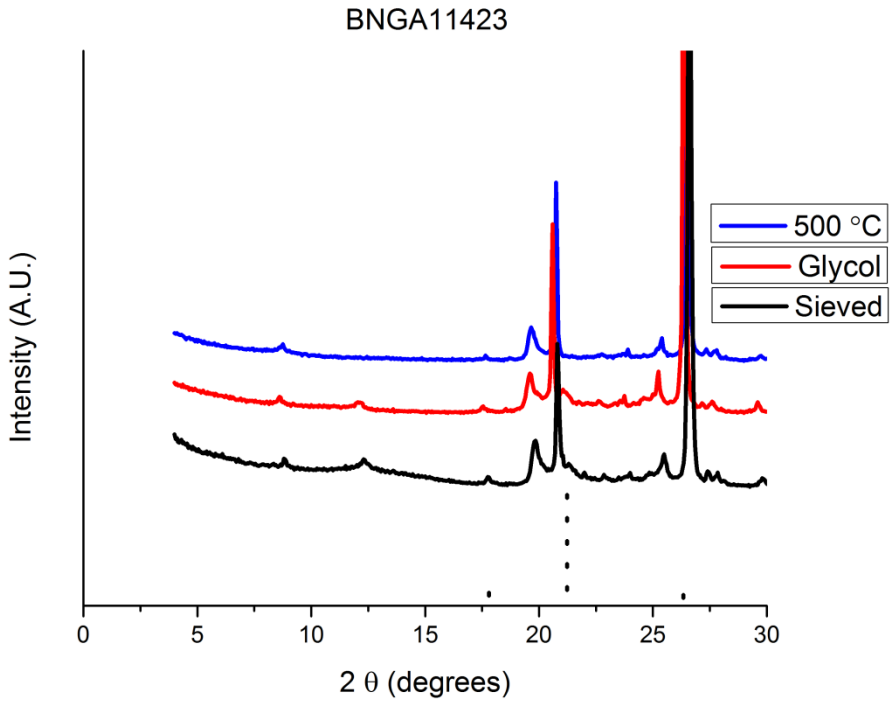
BNGA11423
Intensity (A.U.)
2 θ (degrees)
0
5
10
15
20
25
30
500 °C
Glycol
Sieved

P

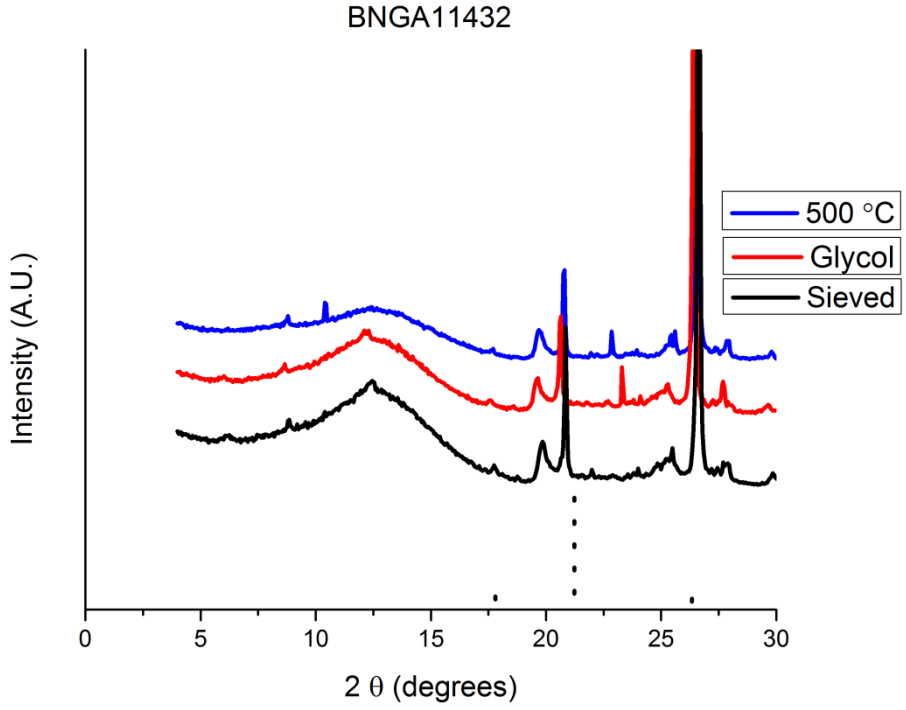
BNGA11432
Intensity (A.U.)
2 θ (degrees)
0
5
10
15
20
25
30
500 °C
Glycol
Sieved

Q

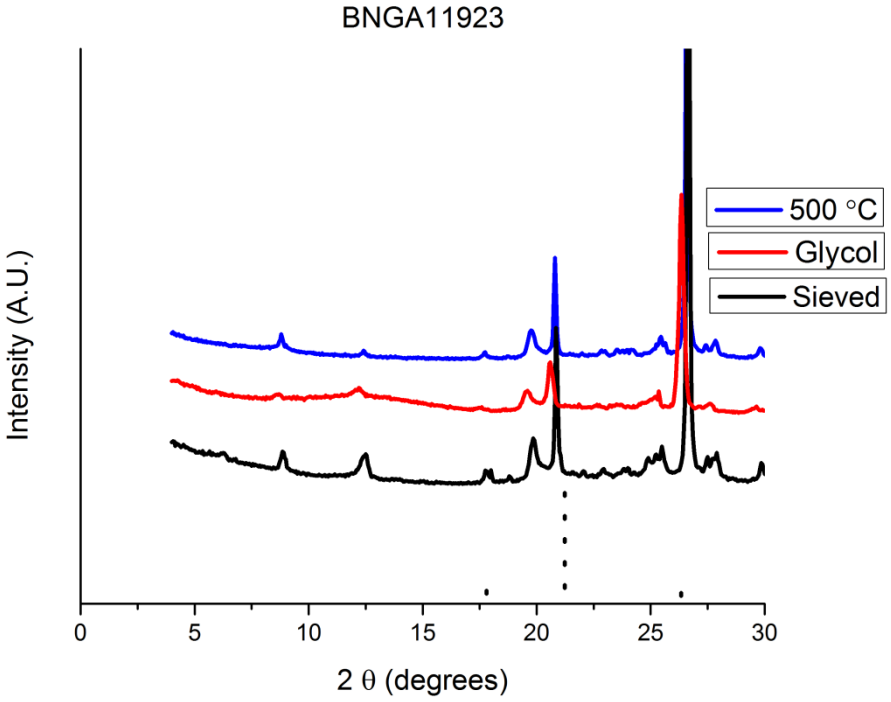
BNGA11923
Intensity (A.U.)
2 θ (degrees)
0
5
10
15
20
25
30
500 °C
Glycol
Sieved

R

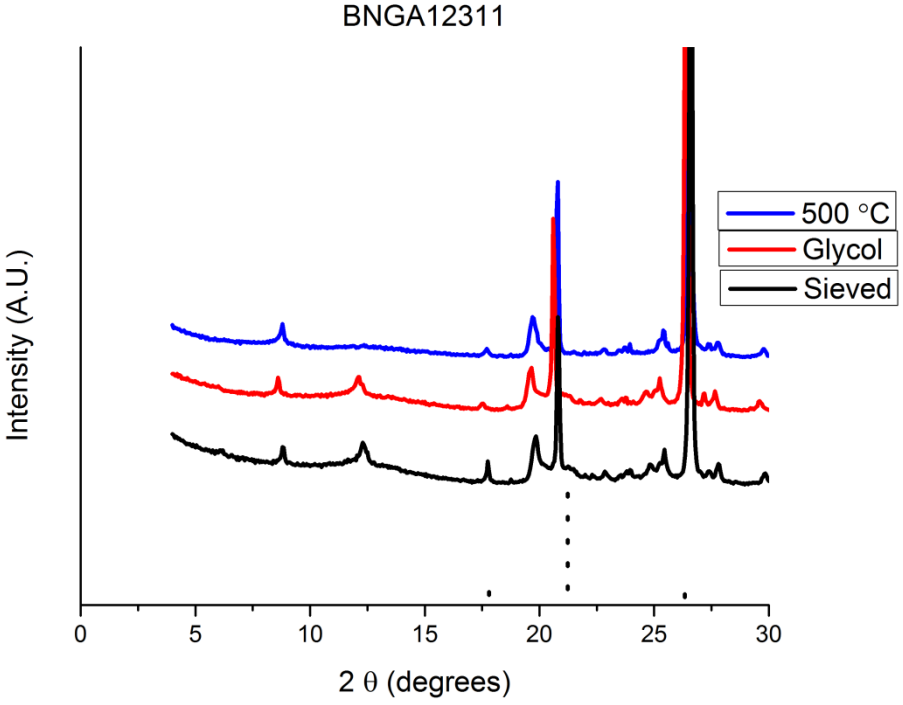
BNGA12311
Intensity (A.U.)
2 θ (degrees)
0
5
10
15
20
25
30
500 °C
Glycol
Sieved

S

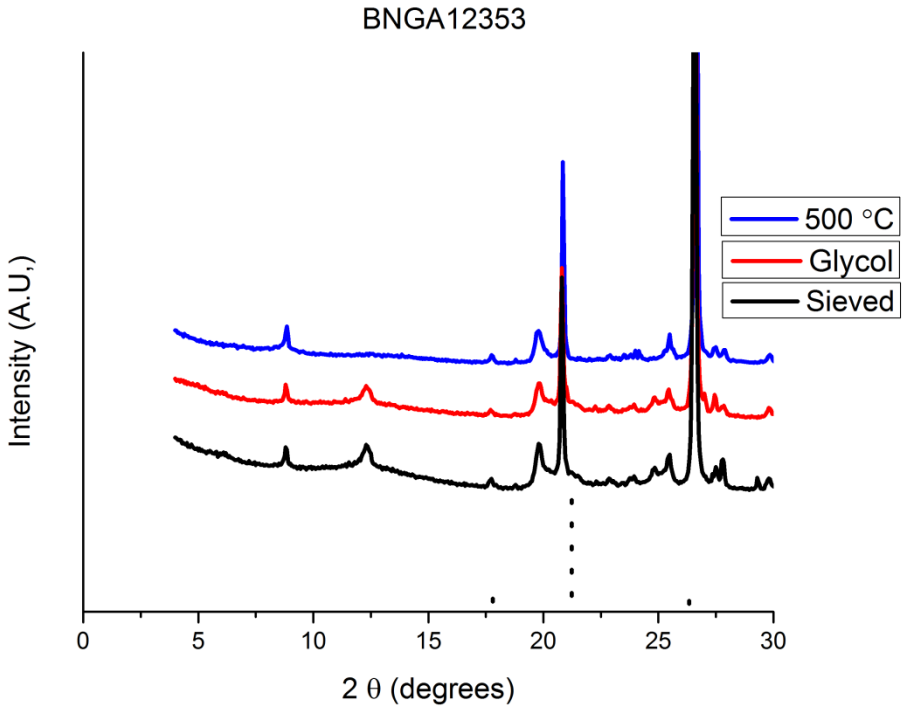
BNGA12353
Intensity (A.U,)
2 θ (degrees)
0
5
10
15
20
25
30
500 °C
Glycol
Sieved

BNGA00202		Peak Position	Area	Area/MIF	% Composition
	Smectite (glycol)	5.2	0	0	0.00
	Illite (air)	8.8	7.11	1.7775	100.00
	Kaolinite (air)	12.3	0		
	Chlorite (cook)	12.3	0	0	0.00
	Kaolinite (difference)	12.3	0	0	0.00
				1.7775	100.00

BNGA00206		Peak Position	Area	Area/MIF	% Composition
	Smectite (glycol)	5.2	3.19	3.19	24.65
	Illite (air)	8.8	12.2	3.05	23.57
	Kaolinite (air)	12.3	13.4		
	Chlorite (cook)	12.3	0	0	0.00
	Kaolinite (difference)	12.3	13.4	6.7	51.78
				12.94	100.00

BNGA00802		Peak Position	Area	Area/MIF	% Composition
	Smectite (glycol)	5.2	5.485	5.485	6.65
	Illite (air)	8.8	164	41	49.71
	Kaolinite (air)	12.3	72		
	Chlorite (cook)	12.3	27.5	13.75	16.67
	Kaolinite (difference)	12.3	44.5	22.25	26.97
				82.485	100.00

BNGA00809		Peak Position	Area	Area/MIF	% Composition
	Smectite (glycol)	5.2	71.7	71.7	98.47
	Illite (air)	8.8	4.47	1.1175	1.53
	Kaolinite (air)	12.3	0		
	Chlorite (cook)	12.3	0	0	0.00
	Kaolinite (difference)	12.3	0	0	0.00
				72.8175	100.00

BNGA00811		Peak Position	Area	Area/MIF	% Composition
	Smectite (glycol)	5.2	0	0	0.00
	Illite (air)	8.8	11.1	2.775	100.00
	Kaolinite (air)	12.3	0		
	Chlorite (cook)	12.3	0	0	0.00
	Kaolinite (difference)	12.3	0	0	0.00
				2.775	100.00

BNGA01402		Peak Position	Area	Area/MIF	% Composition
	Smectite (glycol)	5.2	3.228	3.228	7.01
	Illite (air)	8.8	91.6	22.9	49.70
	Kaolinite (air)	12.3	37.7		
	Chlorite (cook)	12.3	39.9	19.95	43.30
	Kaolinite (difference)	12.3	0		0.00
				46.078	100.00

BNGA05505		Peak Position	Area	Area/MIF	% Composition
	Smectite (glycol)	5.2	0	0	0.00
	Illite (air)	8.8	47.6	11.9	26.86
	Kaolinite (air)	12.3	64.8		
	Chlorite (cook)	12.3	22.9	11.45	25.85
	Kaolinite (difference)	12.3	41.9	20.95	47.29
				44.3	100.00

BNGA05559		Peak Position	Area	Area/MIF	% composition
	Smectite (glycol)	5.2	2.985	2.985	10.65
	Illite (air)	8.8	25.5	6.375	22.75
	Kaolinite (air)	12.3	37.3		
	Chlorite (cook)	12.3	8.415	4.2075	15.02
	Kaolinite (difference)	12.3	28.9	14.45	51.57
				28.0175	100.00

BNGA07105		Peak Position	Area	Area/MIF	% Composition
	Smectite (glycol)	5.2		0	0.00
	Illite (air)	8.8	6.35	1.5875	100.00
	Kaolinite (air)	12.3	0		
	Chlorite (cook)	12.3	0	0	0.00
	Kaolinite (difference)	12.3	0	0	0.00
				1.5875	100.00

BNGA07111		Peak Position	Area	Area/MIF	% Composition
	Smectite (glycol)	5.2	0	0	0.00
	Illite (air)	8.8	7.185	1.79625	100.00
	Kaolinite (air)	12.3	0		
	Chlorite (cook)	12.3	0	0	0.00
	Kaolinite (difference)	12.3	0	0	0.00

				1.79625	100.00
					%
BNGA07235		Peak Position	Area	Area/MIF	Composition
	Smectite (glycol)	5.2	0	0	0.00
	Illite (air)	8.8	9.42	2.355	46.82
	Kaolinite (air)	12.3	5.35		
	Chlorite (cook)	12.3	0	0	0.00
	Kaolinite (difference)	12.3	5.35	2.675	53.18
				5.03	46.82
					%
BNGA09414		Peak Position	Area	Area/MIF	Composition
	Smectite (glycol)	5.2	0	0	0.00
	Illite (air)	8.8	3.54	0.885	100.00
	Kaolinite (air)	12.3	0		
	Chlorite (cook)	12.3	0	0	0.00
	Kaolinite (difference)	12.3	0	0	0.00
				0.885	100.00
					%
BNGA10611		Peak Position	Area	Area/MIF	Composition
	Smectite (glycol)	5.2	10.7	10.7	45.82
	Illite (air)	8.8	14.2	3.55	15.20
	Kaolinite (air)	12.3	18.5		
	Chlorite (cook)	12.3	14.1	7.05	30.19
	Kaolinite (difference)	12.3	4.1	2.05	8.78
				23.35	100.00
					%
BNGA11011		Peak Position	Area	Area/MIF	Composition
	Smectite (glycol)	5.2	0	0	0.00
	Illite (air)	8.8	2.1025	0.525625	14.23
	Kaolinite (air)	12.3	6.3375		
	Chlorite (cook)	12.3	0	0	0.00
	Kaolinite (difference)	12.3	6.3375	3.16875	85.77
				3.694375	100.00
					%
BNGA11023		Peak Position	Area	Area/MIF	Composition
	Smectite (glycol)	5.2	0	0	0.00
	Illite (air)	8.8	3.81	0.9525	19.73
	Kaolinite (air)	12.3	7.75		
	Chlorite (cook)	12.3	2.93	1.465	30.35

	Kaolinite (difference)	12.3	4.82	2.41	49.92
				4.8275	100.00

BNGA11423		Peak Position	Area	Area/MIF	% Composition
	Smectite (glycol)	5.2	0	0	0.00
	Illite (air)	8.8	4.39	1.0975	12.99
	Kaolinite (air)	12.3	14.7		
	Chlorite (cook)	12.3	0	0	0.00
	Kaolinite (difference)	12.3	14.7	7.35	87.01
				8.4475	100.00

BNGA11432		Peak Position	Area	Area/MIF	% Composition
	Smectite (glycol)	5.2	0	0	0.00
	Illite (air)	8.8	2.915	0.72875	8.70
	Kaolinite (air)	12.3	15.3		
	Chlorite (cook)	12.3	0	0	0.00
	Kaolinite (difference)	12.3	15.3	7.65	91.30
				8.37875	100.00

BNGA11923		Peak Position	Area	Area/MIF	% Composition
	Smectite (glycol)	5.2	0	0	0.00
	Illite (air)	8.8	15.4	3.85	17.99
	Kaolinite (air)	12.3	35.1		
	Chlorite (cook)	12.3	4.08	2.04	9.53
	Kaolinite (difference)	12.3	31.02	15.51	72.48
				21.4	100.00

BNGA12311		Peak Position	Area	Area/MIF	% Composition
	Smectite (glycol)	5.2	0	0	0.00
	Illite (air)	8.8	10.8	2.7	16.62
	Kaolinite (air)	12.3	27.1		
	Chlorite (cook)	12.3	0	0	0.00
	Kaolinite (difference)	12.3	27.1	13.55	83.38
				16.25	100.00

BNGA12353		Peak Position	Area	Area/MIF	% Composition
	Smectite (glycol)	5.2	0	0	0.00
	Illite (air)	8.8	10.8	2.7	18.12
	Kaolinite (air)	12.3	24.4		

Chlorite (cook)	12.3	0	0	0.00
Kaolinite (difference)	12.3	24.4	12.2	81.88
			14.9	100.00

Quartz: Clay Ratios

Sample	Q/C ratio
BNGA00202	0.3293
BNGA00206	0.4538
BNGA00802	0.5097
BNGA00809	0.3023
BNGA00811	0.2421
BNGA01402	0.5945
BNGA05505	0.292
BNGA05559	0.301
BNGA07105	0.5903
BNGA07111	0.2793
BNGA07235	0.507
BNGA09414	0.306
BNGA10611	0.4688
BNGA11011	0.4316
BNGA11023	0.2645
BNGA11423	0.445
BNGA11432	0.4
BNGA11923	0.3205
BNGA12311	0.6131
BNGA12353	0.5143

References

1. Jayaraman, S. *et al.* Chromium diboride thin films by low temperature chemical vapor deposition. *J. Vac. Sci. Technol. A* **23,** 631–633 (2005).

2. Petrella, A., Deng, H. & Roberts, N. Single-Source Chemical Vapor Deposition Growth of ZnO Thin Films Using Zn4O(CO2NEt2)6. *Chem. Mater.* **14,** 4339–4342 (2002).

3. Kumar, N., Yang, Y., Noh, W., Girolami, G. S. & Abelson, J. R. Titanium diboride thin films by low-temperature chemical vapor deposition from the single source precursor Ti(BH 4) 3(1,2- dimethoxyethane). *Chem. Mater.* **19,** 3802–3807 (2007).

4. Do, Y. K., Yang, Y., Abelson, J. R. & Girolami, G. S. Volatile magnesium octahydrotriborate complexes as potential CVD precursors to MgB2. Synthesis and characterization of Mg(B3H 8)2 and its etherates. *Inorg. Chem.* **46,** 9060–9066 (2007).

5. Chen, L. *et al.* Growth of CdS nanoneedles by pulsed laser deposition. *J. Electron. Mater.* **41,** 1941–1947 (2012).

6. Rau, J. V *et al.* Superhard tungsten tetraboride films prepared by pulsed laser deposition method. *ACS Appl. Mater. Interfaces* **3,** 3738–43 (2011).

7. Ivanov, B. L., Wellons, M. S. & Lukehart, C. M. Confined-plume chemical deposition: Rapid synthesis of crystalline coatings of known hard or superhard materials on inorganic or organic supports by resonant IR decomposition of molecular precursors. *J. Am. Chem. Soc.* **131,** 11744–11750 (2009).

8. Mohammadi, R. *et al.* Tungsten tetraboride, an inexpensive superhard material. *Proc. Natl. Acad. Sci. U. S. A.* **108,** 10958–10962 (2011).

9. Young, C. E., East, D. & Kaner, R. B. Superhard Materials (ia480). **1,** 1–78

10. Chung, H. Y., Weinberger, M. B., Yang, J. M., Tolbert, S. H. & Kaner, R. B. Correlation between hardness and elastic moduli of the ultraincompressible transition metal diborides RuB#!2, OsB2, and ReB2. *Appl. Phys. Lett.* **92,** 1–3 (2008).

11. Chung, H. Y. *et al.* Synthesis of ultra-incompressible superhard rhenium diboride at ambient pressure. *Science (80-.).* **316,** 436–439 (2007).

12. Orlovskaya, N. *et al.* Mechanochemical synthesis of ReB2 powder. *J. Mater. Res.* **26,** 2772–2779 (2011).

13. Zheng, H. *et al.* Nanostructured tungsten oxide - Properties, synthesis, and applications. *Adv. Funct. Mater.* **21,** 2175–2196 (2011).

14. Deng, H. Characterization of the ZnO thin film prepared by single source chemical vapor deposition under low vacuum condition. *Sci. China Ser. E* **46,** 355 (2003).

15. Weintraub, B., Deng, Y. & Wang, Z. L. Position-Controlled Seedless Growth of ZnO Nanorod Arrays on a Polymer Substrate via Wet Chemical Synthesis. *J. Phys. Chem. C* **111,** 10162–10165 (2007).

16. Choi, D. *et al.* Control of naturally coupled piezoelectric and photovoltaic properties for multi-type energy scavengers. *Energy Environ. Sci.* **4,** 4607 (2011).

17. Wang, Z. L. Self-powered nanosensors and nanosystems. *Adv. Mater.* **24,** 280–285 (2012).

18. Xi, Y. *et al.* Growth of ZnO nanotube arrays and nanotube based piezoelectric nanogenerators. *J. Mater. Chem.* **19,** 9260 (2009).

19. Wu, M. *et al.* A facile hydrothermal preparation and photoluminescence study of ZnO micro/nanostructures on Zn foils. *Sci. China Chem.* **54,** 1547–1551 (2011).

20. Wrobel, G., Piech, M., Gao, P.-X. & Dardona, S. Direct Synthesis of ZnO Nanorod Field Emitters on Metal Electrodes. *Cryst. Growth Des.* **12,** 5051–5055 (2012).

21. Golbeck, J. *The Light-Driven Plastocyanin: Ferredoxin Oxidorreductase*. (Springer, 2006).

22. Gaines, D. F. & Hildebrandt, S. J. New transition metal derivatives of the triborohydride ion and the first example of reversible bidentate-tridentate borane ligand functionality. *J. Am. Chem. Soc.* **96,** 5574–5576 (1974).

23. Bykov, A. Y., Razgonyaeva, G. A., Mal'tseva, N. N., Zhizhin, K. Y. & Kuznetsov, N. T. A new method of synthesis of the B3H8- anion. *Russ. J. Inorg. Chem.* **57,** 471–473 (2012).

24. Halides, C., Cowq, S. R. & Compounds, S. R. Carbonyl Halides of Mangaqzese and Some Related Cowq5ounds. 1601 291. Carbonyl Halides of Manganese and Some Related Compounds. *Carbon N. Y.* **2,** 0–4 (1958).

25. Gaines, D. F. & Hildebrandt, S. J. Syntheses and properties of some neutral octahydrotriborate(1-) complexes of chromium-, manganese-, and iron-group metals. *Inorg. Chem.* **17,** 794–806 (1978).

26. Wahab, R., Ansari, S. G., Kim, Y. S., Dar, M. A. & Shin, H. S. Synthesis and characterization of hydrozincite and its conversion into zinc oxide nanoparticles. *J. Alloys Compd.* **461,** 66–71 (2008).

27. Beam, J. C. *et al.* Construction of a Semiconductor-Biological Interface for Solar Energy Conversion: P-Doped Silicon/Photosystem I/Zinc Oxide. *Langmuir* **31,** 10002–10007 (2015).

28. Van Poppel, L. H., Groy, T. L. & Caudle, M. T. Carbon-Sulfur Bond Cleavage in Bis(N-alkyldithiocarbamato)cadmium(II) Complexes: Heterolytic Desulfurization Coupled to Topochemical Proton Transfer. *Inorg. Chem.* **43,** 3180–3188 (2004).

29. Wang, H. & Ong, C. W. Determination of film-only hardness by eliminating the effects of elastic deformation of substrate. *Surf. Coatings Technol.* **200,** 4433–4439 (2006).

30. Mohammadi, R. *et al.* Enhancing the Hardness of Superhard Transition-Metal Borides: Molybdenum-Doped Tungsten Tetraboride. *Chem. Mater.* **28,** 632–637 (2016).

31. Bauer, J. C., Chen, X., Liu, Q., Phan, T.-H. & Schaak, R. E. Converting nanocrystalline metals into alloys and intermetallic compounds for applications in catalysis. *J. Mater. Chem.* **18,** 275 (2008).

32. Okitsu, K. *et al.* Synthesis of Palladium Nanoparticles with Interstitial Carbon by Sonochemical Reduction of Tetrachloropalladate(II) in Aqueous Solution. *J. Phys. Chem. B* **101,** 5470–5472 (1997).

33. Tao, F. *et al.* Evolution of structure and chemistry of bimetallic nanoparticle catalysts under reaction conditions. *J Am Chem Soc* **132,** 8697–8703 (2010).

34. Cable, R. E. & Schaak, R. E. Low-temperature solution synthesis of nanocrystalline binary intermetallic compounds using the polyol process. *Chem. Mater.* **17,** 6835–6841 (2005).

35. Huang, Y., Zheng, S., Lin, X., Su, L. & Guo, Y. Microwave synthesis and electrochemical performance of a PtPb alloy catalyst for methanol and formic acid oxidation. *Electrochim. Acta* **63,** 346–353 (2012).

36. Kinoshita, K. Particle Size Effects for Oxygen Reduction on Highly Dispersed Platinum in Acid Electrolytes. *J. Electrochem. Soc.* **137,** 845 (1990).

37. Matsumoto, F. Ethanol and Methanol Oxidation Activity of PtPb, PtBi, and PtBi2 Intermetallic Compounds in Alkaline Media. *Electrohemistry* **403,** 333–334 (2012).

38. Rice, C. *et al.* Direct formic acid fuel cells. *J. Power Sources* **111,** 83–89 (2002).

39. Boxall, D. L., Kenik, E. a. & Lukehart, C. M. Synthesis of PtSn/Carbon Nanocomposites Using trans -PtCl(PEt 3) 2 (SnCl 3) as the Source of Metal. *Chem. Mater.* **14,** 1715–1720 (2002).

40. Alden, L. R. *et al.* Synthesis, characterization, and electrocatalytic activity of PtPb nanoparticles prepared by two synthetic approaches. *Langmuir* **22,** 10465–10471 (2006).

41. Ghosh, T. *et al.* PtPb nanoparticle electrocatalysts: Control of activity through synthetic methods. *J. Nanoparticle Res.* **11,** 965–980 (2009).

42. Youn, D. H., Han, S., Bae, G. & Lee, J. S. Carbon-supported PtPb intermetallic compounds for electrooxidation of methyl formate. *Electrochem. commun.* **13,** 806–809 (2011).

43. Delahay, P., Pourbaix, M. & Van Rysselberghe, P. Potential-pH Diagram of Lead and its

Applications to the Study of Lead Corrosion. *J. Electrochem. Soc.* **98,** 101 (1951).

44. Rice, C., Ha, S., Masel, R. I. & Wieckowski, A. Catalysts for direct formic acid fuel cells. *J. Power Sources* **115,** 229–235 (2003).

45. König, R., Schwarze, M., Schomäcker, R. & Stubenrauch, C. Catalytic Activity of Mono- and Bi-Metallic Nanoparticles Synthesized via Microemulsions. *Catalysts* **4,** 256–275 (2014).

46. Ho, C. *et al.* Formation of Sol À Gel-Derived TaO x N y Photocatalysts. 4721–4725 (2011).

47. Steele, B. R. & Vrieze, K. Complexes with metal-carbon bonds, part III(1). Preparation and properties of binuclear diarylplatinum(II) compounds. *Transit. Met. Chem.* **2,** 140–144 (1977).

48. Kuyper, J. Dimethyl Compounds of Platinum (I1). 1 . Oxidative Addition Reactions Involving Group. **2,** 7–12 (1977).

49. Fang, M., Kim, C., Martin, B. & Mallouk, T. Surface Sol–gel Synthesis of Ultrathin Titanium and Tantalum Oxide Films. *J. Nanoparticle Res.* **1,** 43–49 (1999).

50. Boxall, D. L., Deluga, G. a., Kenik, E. a., King, W. D. & Lukehart, C. M. Rapid Synthesis of a PtRu/Carbon Nanocomposite Using Microwave Irradiation: A DMFC Anode Catalyst of High Relative Performance. *Chem. Mater.* **13,** 891–900 (2001).

51. Volpe, D. *et al.* Surface Treatment Effects on the Electrocatalytic Activity and Characterization of Intermetallic Phases. *J. Electrochem. Soc.* **151,** A971 (2004).

52. Casado-Rivera, E. *et al.* Electrocatalytic Activity of Ordered Intermetallic Phases for Fuel Cell Applications. *J. Am. Chem. Soc.* **126,** 4043–4049 (2004).